

Secular Extragalactic Parallax: Measurement Methods and Predictions for Gaia

JENNIE PAINE,¹ JEREMY DARLING,¹ ROMAIN GRAZIANI,^{2,3} AND HÈLÈNE M. COURTOIS²

¹*Center for Astrophysics and Space Astronomy, Department of Astrophysical and Planetary Sciences, University of Colorado, 389 UCB, Boulder, CO 80309-0389, USA*

²*University of Lyon, UCB Lyon 1, CNRS/IN2P3, IP2I Lyon, France*

³*Université Clermont Auvergne, CNRS/IN2P3, Laboratoire de Physique de Clermont, F-63000 Clermont-Ferrand, France*

ABSTRACT

Secular extragalactic parallax caused by the solar system's velocity relative to the cosmic microwave background rest frame may be observable as a dipole proper motion field with amplitude $78 \mu\text{as yr}^{-1}$ Mpc. Nearby galaxies also exhibit proper motions caused by their transverse peculiar velocities that prevent detection of secular parallax for any single galaxy, although a statistical detection may be made instead. Such a detection could constrain the local Hubble parameter. We present methods to measure secular parallax using correlated extragalactic proper motions and find a first limit on the secular parallax amplitude using proper motions of 232 nearby galaxies from *Gaia* Data Release 2. The recovered dipole has insignificant upper limit of $3500 \mu\text{as yr}^{-1}$ Mpc. This measurement will be improved by larger sample size and reduced proper motion uncertainties in future data releases. Using the local peculiar velocity field derived from Cosmicflows-3, we simulate galaxy proper motions and predict that a significant detection ($5 - 10\sigma$) of the secular parallax amplitude will be possible by *Gaia*'s end of mission. The detection is contingent on proper motions of nearby (< 5 Mpc), bright ($G < 15$ mag) galaxies, and corresponds to an insignificant upper limit on the Hubble parameter. We further investigate the implications of our simulations for the study of transverse peculiar velocities, which we find to be consistent with large scale structure theory. The peculiar velocity field additionally results in low-multipole correlated proper motions on the order of $0.3 \mu\text{as yr}^{-1}$ that may be confounded with other cosmological proper motion measurements, such as limits on the gravitational wave background and the anisotropy of the Hubble expansion.

Keywords: Astrometry — Proper motions — Astronomical methods — Observational cosmology — Large-scale structure of the universe

1. INTRODUCTION

A galaxy's proper motion reflects a combination of its peculiar velocity, cosmological effects, and observer induced apparent motions. One such observer induced motion is the secular extragalactic parallax caused by the solar system's velocity with respect to the cosmic microwave background (CMB) rest frame (Kardashev 1986; Ding & Croft 2009; Bachchan et al. 2016). The CMB temperature dipole has an amplitude of about 369 km s^{-1} toward the direction $(l, b) = (264^\circ, 48^\circ)$, $(168^\circ, -7^\circ)$ in RA and Dec., and corresponds to a linear solar velocity of about 78 AU yr^{-1} (Hinshaw et al. 2009). This velocity is a combination of the solar sys-

tem's orbit in the Galaxy and the Galactic peculiar motion and will therefore cause a parallax shift away from the direction of motion for extragalactic objects that is distinct from the annual parallax caused by the Earth's orbit in the solar system. The resulting secular parallax may be observed as a proper motion of amplitude $78 \mu\text{as yr}^{-1} (\frac{1\text{Mpc}}{D}) |\sin \beta|$, where D is the proper motion distance of the galaxy, which is equivalent to the comoving distance for a flat universe (Hogg 1999), and β is the angle between the position of the galaxy and the CMB apex. The global signal is therefore a proper motion dipole that diminishes with distance.

Detection of secular parallax for any individual galaxy is complicated by confounding proper motions. The largest expected contributions to the proper motion are the peculiar velocities caused by gravitational interactions with large-scale structure (LSS) and the secular

aberration drift caused by the solar system barycenter acceleration about the Galactic center. Secular aberration drift is observed as a distance-independent dipole with amplitude of $\sim 5 \mu\text{as yr}^{-1}$ (Titov & Lambert 2013; Triebenbach & Darling 2017), which should be separable from a distance dependent dipole. LSS, however, induces distance-dependent proper motions at all angular scales with amplitudes comparable to secular parallax (Hall 2019). For individual galaxies, separating the peculiar and secular parallax components of the proper motion is not possible without independent estimates of the peculiar velocity and distance of the galaxy, though the inferred secular parallax distance would not provide an independent distance estimate in this case. However, a statistical detection of secular parallax may be possible for large sample of galaxy proper motions, which may be used to calibrate existing extragalactic distance measures and to constrain the Hubble parameter (Ding & Croft 2009; Hall 2019).

To detect the global secular parallax dipole, one needs a large sample of nearby galaxies with proper motion measurements. The *Gaia* mission’s Data Release 2 (DR2) contains proper motions for at least a half million extragalactic objects identified as mid-infrared active galactic nuclei (AGN; Lindegren et al. 2018). Most *Gaia* AGN are either too distant to be useful for secular parallax or may not have distance measures, so in this work we target a new sample of more local galaxies in *Gaia* DR2 using the Cosmicflows-3 catalog (Tully et al. 2016). Individual galaxies should not have significant proper motion measurements from *Gaia*, but with large sample size and even sky distribution, we may constrain correlated proper motions with smaller amplitudes than the individual uncertainties. Future data releases should increase the number of extragalactic objects with measured proper motions and should have substantially lower uncertainties.

The expected secular parallax, peculiar proper motions, and higher multipole signals are detailed in Section 2. We present a first secular parallax limit using *Gaia* DR2 proper motions for a sample of nearby Cosmicflows-3 galaxies in Section 3. In Section 4, we utilize the Cosmicflows peculiar velocity field to simulate galaxy proper motions consistent with *Gaia*’s end-of-mission performance and predict the detection of secular parallax. We analyze the peculiar proper motions in detail in Section 5. Discussion and main conclusions are given in Section 6. We assume a flat cosmology and a Hubble constant of $H_0 = 70 \text{ km s}^{-1} \text{ Mpc}^{-1}$, which is $H_0 = 15 \mu\text{as yr}^{-1}$ in proper motion units.

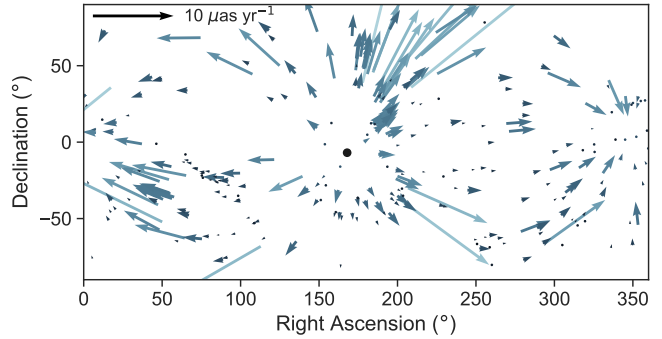


Figure 1. The expected secular parallax proper motions for 232 nearby *Gaia* galaxies, which are described in Section 3.1. The colors of the arrows scale with distance, which range from 3 – 410 Mpc. The direction of the solar system motion with respect to the CMB is indicated by the black dot.

2. CHARACTERIZING THE PROPER MOTION VECTOR FIELD

The term “secular parallax” may have two definitions. The first usage refers to the phenomenon of an apparent distance-dependent dipolar proper motion field caused by the observer’s velocity relative to the bulk motion of a sample of objects. In this work, we use “secular parallax” to describe the proper motion dipole predicted from the solar system’s velocity measured with respect to the CMB reference frame, which may be leveraged to constrain galaxy distances. The former definition includes the dipole correlated components of galaxy velocities with respect to the CMB frame. We distinguish such peculiar proper motions from secular parallax proper motions, although the net dipole one measures is the sum of the two effects. Secular parallax detection as a method to measure galaxy distances or the Hubble constant is contingent on knowing the underlying velocity as a prior, and therefore one must separate the secular parallax from the peculiar transverse motions that are not as well constrained. In this section, we describe the expected secular parallax and other relevant proper motion components.

The global secular parallax field is modeled as a distance-dependent E-mode (curl-free) dipole where galaxies appear to stream away from the direction of motion (Ding & Croft 2009). For example, a galaxy at 1 Mpc and 90° from the CMB apex will have a secular parallax, observed as a proper motion, of $78 \mu\text{as yr}^{-1}$ oriented away from the direction of the CMB dipole apex. The magnitude of the proper motion is modulated by the angle between the galaxy and the direction of the apex, β (Ding & Croft 2009), given by the following expression:

$$|\mu| = (78 \mu\text{as yr}^{-1} \text{ Mpc}) \left(\frac{1}{D} \right) |\sin \beta|. \quad (1)$$

Figure 1 shows the expected parallax dipole proper motions for a sample of *Gaia* galaxies described in Section 3.1 which we use to limit the secular parallax signal.

Following the notation of Mignard & Klioner (2012), an E-mode dipole vector field may be expressed as an $\ell = 1$ vector spherical harmonic:

$$\begin{aligned} \vec{V}_{E1}(\alpha, \delta) = & \sqrt{\frac{3}{4\pi}} (s_{11}^{Re} \sin \alpha + s_{11}^{Im} \cos \alpha) \hat{e}_\alpha \\ & + \sqrt{\frac{3}{4\pi}} \left(s_{10} \sqrt{\frac{1}{2}} \cos \delta + s_{11}^{Re} \cos \alpha \sin \delta \right. \\ & \left. - s_{11}^{Im} \sin \alpha \sin \delta \right) \hat{e}_\delta \end{aligned} \quad (2)$$

where the coefficients s_{10} and $s_{11}^{Re,Im}$ determine the direction and amplitude of the vector field, and α and δ are the coordinates in RA and Dec. The vectors \hat{e}_α and \hat{e}_δ are unit vectors in RA and Dec. The power of the vector field is the integral of the squared field over the unit sphere and is calculated from the coefficients by

$$P_{E1} = s_{10}^2 + 2 \left((s_{11}^{Re})^2 + (s_{11}^{Im})^2 \right). \quad (3)$$

The power is related to the dipole amplitude by

$$A_{E1} = \sqrt{\frac{3}{8\pi} P_{E1}}, \quad (4)$$

where the factor of $\sqrt{3/8\pi}$ comes from integrating over 4π sr.

The distance dependence of secular parallax may be incorporated by expressing the coefficients in units of $\mu\text{as yr}^{-1}$ Mpc (velocity units). The solar system's velocity with respect to the CMB is $369 \pm 0.9 \text{ km s}^{-1}$ in the direction $(l, b) = (264^\circ, 48^\circ)$ (Hinshaw et al. 2009), which causes an observed proper motion dipole with coefficients $(s_{10}, s_{11}^{Re}, s_{11}^{Im}) = (27.2, -155.0, -33.1) \mu\text{as yr}^{-1}$ Mpc. The secular parallax dipole root power is $\sqrt{P_{E1}} = 226 \mu\text{as yr}^{-1}$ Mpc and the amplitude is $78 \mu\text{as yr}^{-1}$ Mpc, as given by Equation 1.

Two other E-mode dipolar proper motions of interest in this work are the secular aberration drift and the peculiar proper motion dipole caused by LSS. The former is a distance-independent dipole that has been previously detected using quasar proper motions from very long baseline interferometry (Titov & Lambert 2013; Truebenbach & Darling 2017). The secular aberration drift amplitude is $\sim 5 \mu\text{as yr}^{-1}$, which will dominate dipolar proper motions for galaxies at distances of approximately 16 Mpc or greater. We expect that the secular aberration drift will be detected with *Gaia* using high redshift AGN (Paine et al. 2018), enabling the study of distance-dependent dipoles after the distance-independent signal is subtracted.

Peculiar velocities induce distance-dependent proper motions at all angular scales, including a dominant dipole for local galaxies. Hall (2019) presented predictions for the LSS transverse velocity power spectrum and its correlation to the secular parallax dipole. The transverse peculiar velocity dipole causes proper motions of similar amplitude to secular parallax for galaxies within ~ 100 Mpc. Hall (2019) therefore predict transverse peculiar velocities dominate the error on secular parallax measurements for local galaxies. The predicted peculiar velocity dipole decreases in power as a function of distance, which causes the observed peculiar proper motion dipole amplitude to decrease faster than $1/D$. The distance dependence of peculiar proper motions means that the peculiar dipole may not be fit separately and subtracted prior to fitting for secular parallax, unlike the secular aberration drift.

In Section 5, we investigate higher multipole vector fields associated with peculiar proper motions. Expressions for $\ell = 2, 3$ vector fields may be found in Mignard & Klioner (2012). The power for any general ℓ is

$$P_\ell = s_{\ell 0}^2 + t_{\ell 0}^2 + 2 \sum_{m=1}^{\ell} \left((s_{\ell m}^{Re})^2 + (s_{\ell m}^{Im})^2 + (t_{\ell m}^{Re})^2 + (t_{\ell m}^{Im})^2 \right), \quad (5)$$

where s and t denote the spheroidal (E-mode) and toroidal (B-mode) components of the vector field, respectively.

The total proper motion field is then the vector sum of distance-dependent and distance-independent components:

$$\begin{aligned} \vec{\mu}(D) = & \vec{V}_{E1,SP} D^{-1} + \vec{V}_{E1,PV} D^{-1} \\ & + \sum_{\ell=2}^{\infty} \left(\vec{V}_{E\ell,PV} D^{-1} + \vec{V}_\ell \right), \end{aligned} \quad (6)$$

where $\vec{V}_{E1,SP}$ denotes the dipole induced by the solar system velocity with respect to the CMB. $\vec{V}_{E1,PV}$ and $\vec{V}_{E\ell,PV}$ denote the dipole and higher order E-modes induced by peculiar velocities. The secular aberration drift and higher order distance-independent modes are represented by \vec{V}_ℓ . Note that the secular parallax and peculiar components have units of velocity, $\mu\text{as yr}^{-1}$ Mpc, whereas the distance-independent multipoles are given in units of proper motion, $\mu\text{as yr}^{-1}$.

3. A FIRST SECULAR PARALLAX LIMIT

3.1. Sample Selection

Making a statistical detection of extragalactic parallax will require a large sample of nearby galaxies with both proper motion and distance measurements. For this

purpose, we selected galaxies from Cosmicflows-3 (Tully et al. 2016), a catalog of 17,669 redshift-independent galaxy distances. The majority of distances were measured using either the relation between galaxy rotation and luminosity (the Tully-Fisher relation; Tully & Fisher 1977) or the relations between the velocity dispersion, radius, and luminosity of elliptical galaxies (the fundamental plane; Djorgovski & Davis 1987; Dressler et al. 1987). Redshift based distance estimates are more widely available for galaxies detected by *Gaia*. However, the accuracy of redshift based distance estimates is diminished for relatively small distances because the recession velocity predicted by the Hubble flow is comparable to typical radial peculiar velocities. Such estimates are therefore inappropriate for very nearby galaxies (< 10 Mpc) that will show the largest observer induced proper motions. Additionally, the Cosmicflows-3 catalog includes line-of-sight peculiar velocity measurements, which Graziani et al. (2019) used to derive the local peculiar velocity field and matter distribution. In Section 4, we employ these peculiar velocities to forecast the detection of secular parallax in future *Gaia* data releases

We cross-matched Cosmicflows-3 with *Gaia* DR2 using a 3 arcsecond matching radius, which resulted in 9,823 objects. We performed cuts of the sample in order to mitigate contamination from Galactic stars, which will typically have larger, more significant proper motions than those expected for galaxies. We excluded any sources within 10 degrees of the Galactic plane ($|b| \leq 10^\circ$), and any remaining sources with significant annual parallaxes measured by *Gaia* ($|p| \geq 5\sigma_p$). Finally, we removed galaxies within 1.5 Mpc, approximately the radius of the Local Group. The resulting catalog contains 9,699 galaxies, of which only 429 have a full 5-parameter astrometric solution (measured position, parallax, and proper motion) in *Gaia* DR2. We use only these 429 galaxies with proper motion measurements below. In Section 4, we utilize the larger sample, including sources without proper motion measurements, to simulate end-of-mission proper motions and predict detection of the secular parallax dipole.

3.1.1. Visual Inspection

Parallax induces the largest proper motions in nearby galaxies, but nearby galaxies are not point-like. However, extended objects did not receive special treatment in the data processing for *Gaia* DR2 and were treated as single stars in the astrometric solution (Gaia Collaboration et al. 2018a). To ensure that the *Gaia* positions and proper motions are reasonable, we visually inspected all 429 galaxies using Sloan Digital Sky Survey

(SDSS) g-band imaging where available, or images from the Digitized Sky Survey II (DSS-II). Each image was examined for potentially problematic features, including extended galaxies without a clear centroid or off-center *Gaia* positions. Examples of such galaxies are shown in Figure 2. In cases where SDSS imaging was not available and the *Gaia* position appeared marginal from DSS-II images, other images from the literature were examined. Nearby galaxies (< 50 Mpc) received more scrutiny than more distant ones, since the proper motions of nearby objects provide a larger contribution to the secular parallax signal. The majority of the galaxies in our initial cross-match are extended, however only 119 were identified as extended with a poor *Gaia* position and were removed from the sample. We identified an additional 6 *Gaia* positions where there were no visible sources as well as one foreground star, which were removed from the sample. The resulting catalog contains 303 galaxies which pass visual inspection.

3.1.2. Proper Motion and Distance Clipping

Out of the 303 remaining objects, 242 have proper motion amplitudes greater than 1 mas yr^{-1} , at least an order of magnitude larger than the expected proper motions caused by either secular parallax or a galaxy’s peculiar motions. 71 of these galaxies have $> 5\sigma$ proper motions in RA and/or Dec. As a result, an initial error-weighted fit of the parallax dipole (Equation 2) to the sample has a non-significant amplitude (defined by Equation 4) of $32 \pm 8 \text{ mas yr}^{-1} \text{ Mpc}$. Significant proper motions of galaxies are most likely either spurious measurements or foreground stars that were missed during visual inspection, so we remove any sources with $> 5\sigma$ proper motions in either RA or Dec. The proper motions and positions of the remaining 232 galaxies are shown in Figure 3, and their distances and G magnitudes are shown in Figure 4.

To understand the sensitivity of our fitting technique to the remaining large, but insignificant proper motions, we tested the parallax model on the sample with a range of maximum proper motion vector amplitude¹ cutoffs between 0.1 and 5 mas yr^{-1} . For each proper motion cutoff, we fit a distance dependent E-mode dipole using least-squares minimization. None of the fits are significant and the coefficients are generally consistent with zero. For each cut we find the 95% confidence interval upper limit for the dipole amplitude via Monte Carlo sampling of the fit coefficients. The top plot of Figure 5

¹ Proper motion amplitudes are calculated by $|\mu| = \sqrt{\mu_{\alpha*}^2 + \mu_{\delta}^2}$, where $\mu_{\alpha*} = \mu_{\alpha} \cos \delta$, and μ_{α} and μ_{δ} are the proper motion in the RA and Dec directions, respectively.

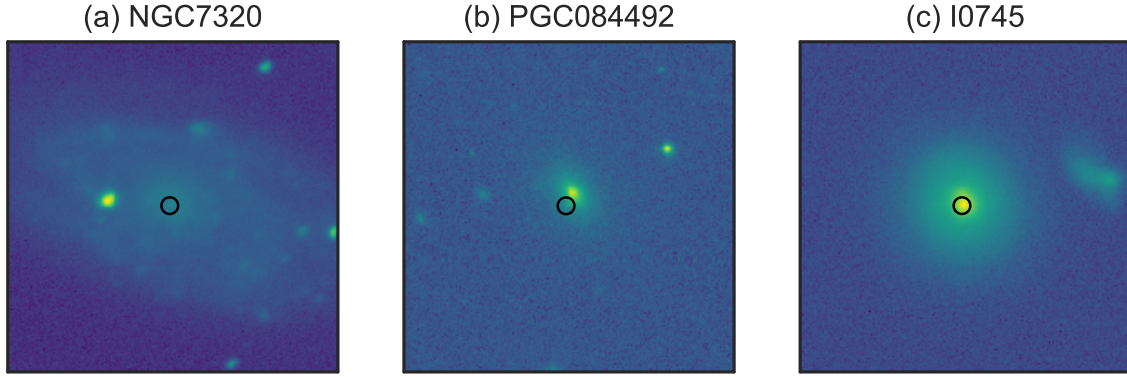


Figure 2. SDSS g -band images of three extended galaxies demonstrating examples of the visual criteria used to verify *Gaia* positions. Circles indicate the *Gaia* position for each galaxy and are each 2 arcsec in radius (typical position errors for objects in our sample are 0.5 mas). (a) A galaxy with no core. (b) A galaxy where the *Gaia* position is off-center. (c) An example of an extended galaxy with an acceptable *Gaia* position.

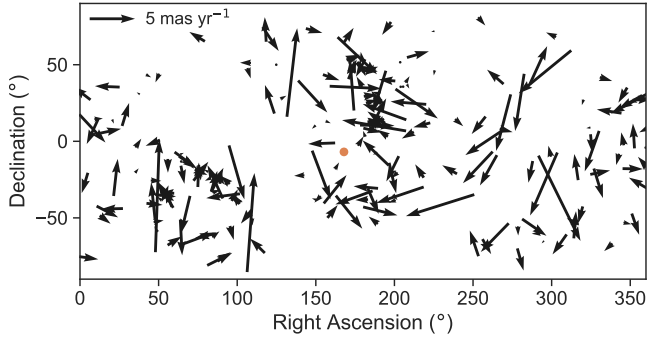


Figure 3. Proper motions and sky distribution of our sample of 232 *Gaia*-Cosmicflows galaxies. Note that none of the proper motions shown are significant. The coordinates are located at the midpoint of each arrow. The direction of the solar system motion with respect to the CMB is indicated by the orange dot. Apparent clustering of arrows is due to the exclusion of objects within 10 degrees of the Galactic plane.

shows the amplitude upper limit vs. maximum proper motion amplitude in the fit sample. Note that the fit amplitudes are expressed in mas yr^{-1} , so the fits are at least an order of magnitude larger than the expectation. The variability below the 1 mas yr^{-1} cut off may be attributed to small sample sizes. The amplitude upper limit for the fit to the sample with no maximum proper motion cutoff is $\sim 3.5 \text{ mas yr}^{-1} \text{ Mpc}$, and we find only a marginal reduction in the limit for proper motion cutoffs around $1\text{-}4 \text{ mas yr}^{-1}$.

Our galaxy sample includes objects at distances up to 410 Mpc, most of which have expected secular parallax proper motions smaller than a few $\mu\text{as yr}^{-1}$ and should not contribute greatly to the global parallax signal relative to the more numerous nearby galaxies. However, the systematics that dominate the *Gaia* DR2 proper motions for this sample are distance-independent, so fits of the distance-dependent dipole may be sensitive to dis-

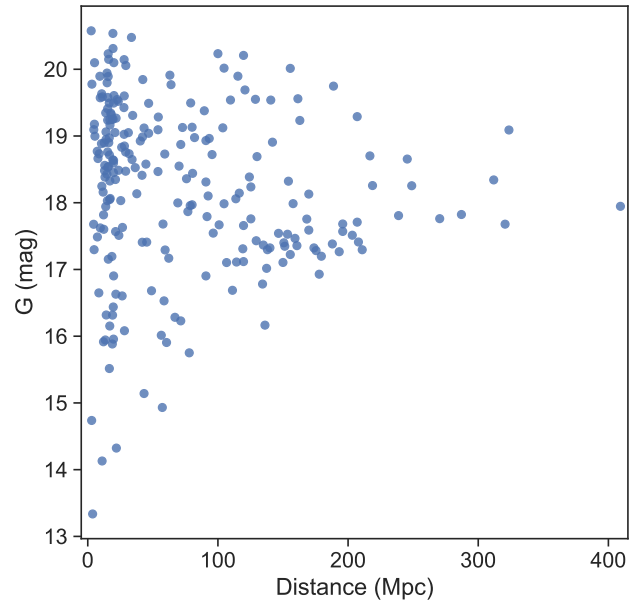


Figure 4. G magnitudes vs. distance for our sample of 232 *Gaia*-Cosmicflows galaxies. *Gaia* proper motion uncertainties scale with magnitude.

tance binning. In particular, we want to test whether the inclusion of galaxies at large distances may bias the best-fit amplitudes to larger values due to the dominant systematic errors. The bottom plot of Figure 5 shows the same varying maximum proper motion fits described above for three choices of maximum distance: 20, 50, and 100 Mpc. Again we find only small differences between cuts, except for low distance and proper motion cuts where the sample size is small. Conversely, increasing the minimum distance of the sample consistently increases the best-fit amplitudes and uncertainties. The fits are therefore most sensitive to the proper motions of the nearest galaxies in the sample, with little to no im-

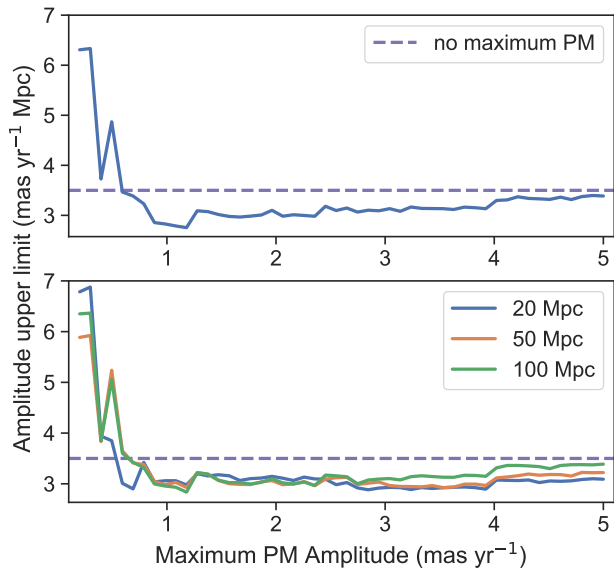


Figure 5. Top: dipole amplitude upper limits vs. maximum proper motion amplitude for the sample within 410 Mpc. The purple dashed line is the upper limit for the sample with no maximum proper motion cut off. The sample size for the maximum cut off is 213 objects, whereas the sample size for cut offs $< 0.8 \text{ mas yr}^{-1}$ is between 6 and 44 objects. Bottom: Same as top for maximum distance cutoffs of 20, 50, and 100 Mpc. The purple dashed line is the upper limit for the sample with no maximum proper motion or distance cut offs.

provement on the limit from increasing the sample size by including distant galaxies.

We next consider the impact that cluster member galaxies may have on these fits, as galaxies in clusters can have peculiar velocities on the order of 1000 km s^{-1} and may result in proper motions that are correlated with other members of the same cluster. Three nearby clusters are represented in our sample: Virgo (14 galaxies), Ursa Major (6 galaxies), and Fornax (12 galaxies). At approximately the distance of the Virgo cluster, a peculiar transverse velocity of 1000 km s^{-1} would correspond to a $\sim 15 \mu\text{as yr}^{-1}$ proper motion, well below the statistical and systematic errors in the sample. If we exclude all cluster members from the sample, we find a dipole amplitude upper limit of $\sim 3.5 \mu\text{as yr}^{-1} \text{ Mpc}$, confirming that cluster members are not the source of the large amplitudes discussed previously.

We therefore conclude that further cuts on the catalog do not significantly improve the secular parallax limit. In Section 3.2, we present details on this limit using the proper motions displayed in Figure 3.

3.2. Results

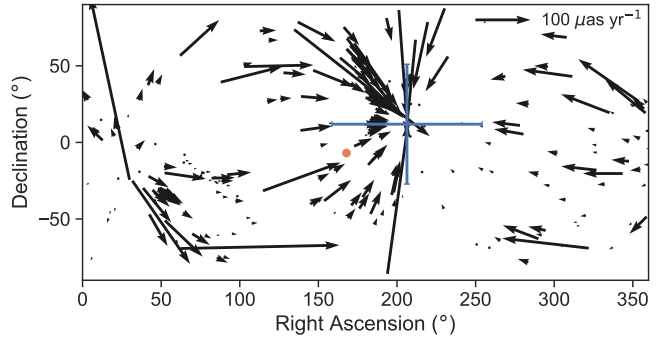


Figure 6. Best fit distance dependent dipole to the proper motions of our sample of 232 nearby galaxies (Figure 3). Note that this dipole is not significant. The blue cross shows the location and uncertainty of best fit antapex. The direction of the solar system motion with respect to the CMB is indicated by the orange dot.

We fit a distance dependent E-mode dipole to the proper motions of our sample of 232 galaxies using least-squares fitting. The best fit dipole is $(s_{10}, s_{11}^{Re}, s_{11}^{Im}) = (800 \pm 3300, 2400 \pm 2100, -1200 \pm 1800) \mu\text{as yr}^{-1} \text{ Mpc}$, which results in a 95% confidence interval upper limit on the dipole amplitude of $\sim 3500 \mu\text{as yr}^{-1} \text{ Mpc}$. The best fit proper motions are shown in Figure 6. The dipole is not significant, but it is coincidentally nearly anti-aligned with the expected dipole.

The limit is about an order of magnitude larger than either the expectation from the solar system’s velocity or the peculiar velocities of nearby galaxies. It therefore represents an insignificant upper limit on the velocity of the solar system with respect to the bulk peculiar flow. For an estimate of H_0 , one needs only the component of the proper motion caused by the velocity with respect to the CMB, which may be estimated by fixing the dipole direction to the CMB dipole apex. The unfixed dipole is nearly anti-aligned with the CMB dipole, so the fixed-direction fit has zero amplitude. The uncertainties on dipole coefficients $(s_{10}, s_{11}^{Re}, s_{11}^{Im})$ are $(270, 1500, 320) \mu\text{as yr}^{-1} \text{ Mpc}$, and the 95% confidence upper limit on the amplitude is $\sim 1500 \mu\text{as yr}^{-1} \text{ Mpc}$. The fractional uncertainty of the amplitude may be translated to H_0 , which implies an H_0 limit of $1400 \text{ km s}^{-1} \text{ Mpc}^{-1}$. We note that we do not measure an H_0 limit; rather it is an estimate of the limit that may be achieved using current *Gaia* data.

The large scale systematics in *Gaia* DR2 proper motions are of the order $40 \mu\text{as yr}^{-1}$ for angular scales $\gtrsim 18^\circ$ (Lindegren et al. 2018; Gaia Collaboration et al. 2018b). Further, Gaia Collaboration et al. (2018b) find that the dipole systematic proper motion effects are of the order of $10 \mu\text{as yr}^{-1}$ for their *Gaia* celestial reference frame quasar sample. To assess the large scale

systematics present in our sample of 232 galaxies, we fit a distance-independent E1 dipole to the sample. We find an insignificant dipole of $(s_{10}, s_{11}^{Re}, s_{11}^{Im}) = (280 \pm 210, 360 \pm 170, -80 \pm 160) \mu\text{as yr}^{-1}$, which corresponds to $200 \pm 80 \mu\text{as yr}^{-1}$ amplitude. The apex directions of the distance-dependent and independent fits are consistent, indicating that both fits probe the same underlying systematics. Additionally, the distance-dependent dipole amplitude normalized to the median distance of the sample, 43 Mpc, is $\sim 30 \mu\text{as yr}^{-1}$, which is consistent with the known *Gaia* systematics.

Either an improvement of the statistical and systematic errors or a larger sample size will therefore be required to reduce the uncertainty of the secular parallax limit. The uncertainty on the coefficients and amplitude of the global signal scales with the sample size as $N^{-1/2}$, so to achieve uncertainty on the signal at 1 Mpc of about $10 \mu\text{as yr}^{-1}$ without any reduction on the individual proper motion uncertainties would require a larger sample size by a factor of 10,000, assuming identical distance and sky distributions. However, proper motion uncertainties scale as $t^{-3/2}$, so the longer time baseline of future *Gaia* data releases will decrease the individual uncertainties. The average per-object uncertainties will decrease by about an order of magnitude by *Gaia*'s nominal end of mission. For the sample used to make the above limit, the mean expected uncertainties are ~ 120 and $110 \mu\text{as yr}^{-1}$ in RA and Dec.

4. SECULAR PARALLAX PREDICTIONS

As demonstrated in the previous section, the systematics present in *Gaia* DR2 act as a noise floor below which we may not analyze low multipole proper motions. Future *Gaia* data releases, however, will likely contain larger numbers of extragalactic proper motion measurements with lower per object statistical uncertainties and systematics. We can expect that the majority of the 9,823 objects in our initial *Gaia*-Cosmicflows crossmatch will have proper motion measurements by the final data release. In this section, we therefore forecast the detectability of secular parallax for *Gaia* end-of-mission astrometry and explore the ideal sample selection to be used for future data releases.

4.1. Simulated Proper Motion Catalog

We calculate proper motions consistent with *Gaia*'s expected end-of-mission performance for objects in the *Gaia*-Cosmicflows crossmatch described in Section 3.1. We exclude any galaxies closer than 1.5 Mpc, with galactic latitude below 10 degrees, or with significant annual parallax detected by *Gaia*. The later two requirements mitigate contamination by foreground stars. One additional object was identified as a foreground star by visual

inspection. The catalog contains 9,698 objects, most of which do not have measured proper motions as of *Gaia* DR2. For each galaxy, we simulate a *Gaia* end-of-mission proper motion based on three components: the source's predicted proper motion errors, the expected secular parallax, and predicted peculiar velocity based on the Cosmicflows-3 peculiar velocity field.

End-of-mission proper motion errors are calculated using the PyGaia Python toolkit.² The predicted uncertainties assume a five year mission, although *Gaia*'s total mission lifetime has already passed its nominal five years (Gaia Collaboration et al. 2016). The calculation depends on the source's G magnitude, ecliptic latitude, and $V - I_C$ color. We set the latter to zero for all sources as the color has negligible impact on the predicted uncertainty and is not available for all sources. The mean expected uncertainties are $77 \mu\text{as yr}^{-1}$ for proper motion in R.A. and $68 \mu\text{as yr}^{-1}$ in Dec. Note that the predicted uncertainties do not include potential systematic errors. We generate proper motion noise for each object by randomly sampling from a Gaussian distribution with standard deviation set to the object's predicted proper motion uncertainty in R.A. and Dec.

Peculiar proper motions are calculated from the local peculiar velocity field described in detail in Graziani et al. (2019). The velocity field was reconstructed from the Cosmicflows-3 catalog, utilizing the observed distance moduli and redshifts of Cosmicflows galaxies to infer both the matter over-density field and the three-dimensional peculiar velocity field. We find peculiar proper motions then by converting the transverse velocities to angular motions. The transverse velocities are on the order of a few hundred km s^{-1} in the CMB frame, with a maximum of $\sim 1000 \text{ km s}^{-1}$. The resulting peculiar proper motions range from 0.005 to $60 \mu\text{as yr}^{-1}$ and the mean is $\sim 1 \mu\text{as yr}^{-1}$.

In Figure 7, we plot the peculiar vs. secular parallax proper motions (calculated from Equation 2) for each galaxy. The peculiar proper motion amplitude is larger than the expected secular parallax for 58% of galaxies in the sample. While the transverse velocity amplitudes of individual galaxies do not depend on distance, the corresponding peculiar angular motions depend on distance as $1/D$, which complicates the measurement of secular parallax. Additionally, the transverse velocity angular power spectrum varies with distance, with more power in $\ell = 1$ at smaller distances (Hall 2019; Section 5.1).

To create the simulated proper motion catalog, we first sample each object's end-of-mission uncertainties

² www.cosmos.esa.int/web/gaia/science-performance

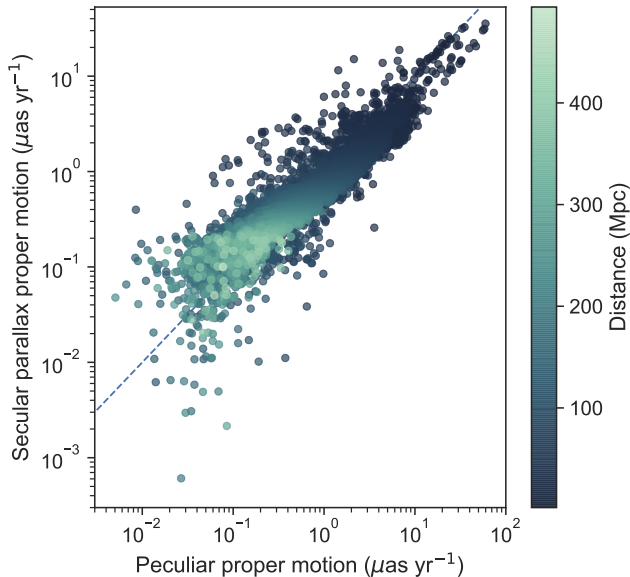


Figure 7. Simulated secular parallax vs. peculiar proper motion components for individual objects. Colors scale with the distance of each galaxy. For reference, the dashed line denotes a one-to-one correspondence where peculiar proper motions show the same amplitude (but not necessarily direction) as the secular parallax.

to generate a noise term, and then add the predicted parallax and peculiar proper motions. We note that the largest contribution to real extragalactic proper motions is typically the secular aberration drift, which we do not include in our simulations in this work. However, the secular aberration drift is expected to be measured with high significance using the sample of $> 5 \times 10^5$ AGN detected by *Gaia* (Paine et al. 2018). The following predictions are therefore made with the assumption that the secular aberration drift dipole can be constrained or subtracted prior to fitting for secular parallax. We also do not include the effects of possible contaminating foreground stars; the proper motion is calculated assuming that each *Gaia* source is the Cosmicflows galaxy.

4.2. *Gaia* End of Mission Simulations

To simulate secular parallax detection, we perform error weighted least squares fits of the distance-dependent dipole model to the simulated proper motion catalog. We perform 1,000 fits, where for each trial we generate random noise for each object by sampling the end-of-mission uncertainties. The average resulting fit is a $107 \pm 12 \mu\text{as yr}^{-1}$ Mpc dipole with apex of $(195 \pm 6^\circ, 22 \pm 7^\circ)$ in RA and Dec, and mean Z-score of 7.8. The mean dipole coefficients are listed in Table 1. The average best-fit dipole is significantly offset from the secular parallax expectation from the CMB, which is due to

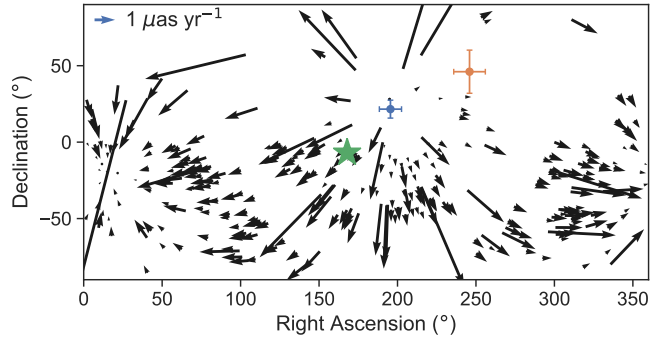


Figure 8. Arrows show the simulated best fit dipole for the proper motions including secular parallax, peculiar motions, and noise consistent with *Gaia* end-of-mission uncertainties. The midpoint of the arrows represent the coordinates of 300 objects randomly selected from the simulated catalog to illustrate the proper motion vector field. The blue cross shows the location of the apex of the fit, whereas the orange cross shows the location of the apex when fitting to the peculiar proper motions alone, and the green star is the location of the CMB apex and the apex of the secular parallax dipole. The offset of the best fit dipole from the CMB apex demonstrates the mixing of the peculiar and parallax dipoles.

dipole correlations of the peculiar proper motions in our sample. For each trial, we also perform fits to the catalog excluding the predicted secular parallax proper motions, in order to demonstrate the impact of peculiar motions on secular parallax detection. The mean dipole coefficients for the noisy peculiar proper motions are also listed in Table 1 and correspond to a $69.1 \pm 11.6 \mu\text{as yr}^{-1}$ Mpc dipole toward $(246 \pm 14^\circ, 46 \pm 10^\circ)$. The dipole detected in the full simulation reflects the combination of the expected secular parallax and peculiar proper motions. In fact, the best-fit dipole parameters are consistent with the sum of the separate parallax and peculiar dipole parameters, and the amplitude is consistent with the parallax and peculiar dipole amplitudes summed in quadrature. The mixing of the two dipoles is further demonstrated in Figure 8, which shows the locations of the best-fit dipole apex for the full simulation, for the peculiar proper motions, and the expected secular parallax apex (CMB apex).

From Equation 2, one can demonstrate that the vector field produced by addition of two dipoles is simply another dipole. It is therefore not possible to separate the parallax and peculiar dipoles observationally without prior knowledge of either component. However, the CMB dipole has a well measured direction, so we may fix the location of the dipole apex in order to recover the secular parallax amplitude. This is achieved by constraining the ratios of s_{10} to s_{11}^{Re} and s_{11}^{Im} while fitting (the signs and relative absolute values of the coefficients determine the direction of the dipole, whereas the sum

	s_{10}	s_{11}^{Re}	s_{11}^{Im}	Amplitude	Apex coordinates
	($\mu\text{as yr}^{-1}$ Mpc)	($\mu\text{as yr}^{-1}$ Mpc)	($\mu\text{as yr}^{-1}$ Mpc)	($\mu\text{as yr}^{-1}$ Mpc)	RA, Dec
Secular Parallax	27.2	-155	-33.1	78	167.9°, -6.9°
Peculiar	-139(38)	-38.9(24.0)	86.9(20.3)	69.1(11.6)	245.9°, 46.1°
Full simulation	-112(38)	-194(24)	53.8(20.3)	107(12)	195.5°, 21.6°

Table 1. Dipole properties for the expected secular parallax dipole, the best-fit dipole to simulated peculiar proper motions, and the best-fit dipole to the full simulation including secular parallax, peculiar, and random noise proper motion components.

of squares gives the amplitude as in Equations 3-4). We perform 1,000 trials fitting the fixed-direction distance-dependent dipole, again randomly generating noise for each trial. The resulting average fit has amplitude $\sim 74 \mu\text{as yr}^{-1}$ Mpc detected with mean Z-score of 9.5. This represents a significant detection of the secular parallax amplitude. We note that the peculiar proper motion dipole is nearly orthogonal to the expected secular parallax dipole and therefore contributes almost zero amplitude to the fixed-direction fits. The orthogonality of the two components is a fortunate coincidence due to the solar system’s phase in its Galactic orbit and the Galaxy’s peculiar motion.

Finally, we test the possibility of constraining both the parallax and peculiar dipoles. We perform 1,000 trials simultaneously fitting two distance-dependent dipoles, one with direction fixed to the CMB apex and one with variable direction and amplitude. Neither dipole is recovered when simultaneously fitting, so it will be necessary to account for the secular parallax dipole prior to studying the peculiar proper motions from LSS. This may be achieved by either fitting for the parallax dipole independently as described above and subtracting the detected field, or assuming the secular parallax proper motion field from the CMB.

4.2.1. Predicted Dependence on Sample Selection

The 9σ detection prediction is made for nearly the full *Gaia*-Cosmicflows sample, only employing cuts on the sample to mitigate stellar contamination and poor centroid fits. However, the predicted detection is very sensitive sample selection. Below, we consider several variables that may impact the detection: the minimum and maximum distances, D_{min} and D_{max} ; maximum individual proper motion amplitude; and minimum G magnitude.

The choice of D_{min} should impact the relative contribution of the peculiar proper motions to the detected dipole since the peculiar velocity dipole decreases in power for larger distances (Hall 2019, see also Section 5.1). The peculiar dipole is approximately orthogo-

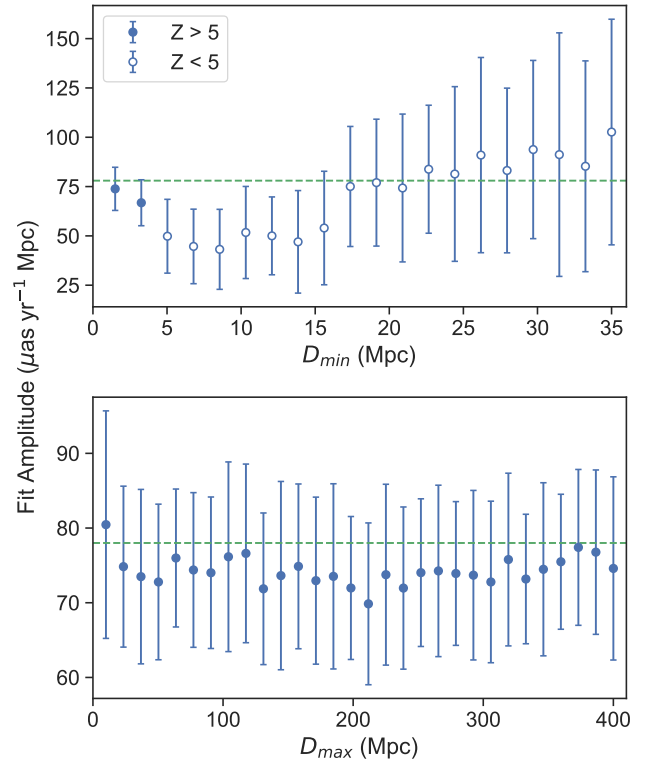


Figure 9. Simulated fixed-direction, distance-dependent dipole fits for minimum distance cuts between 1.5 and 35 Mpc (top) and for maximum distance cuts between 10 and 400 Mpc (bottom). Fits are made to the simulated proper motions including expected secular parallax, model predicted peculiar motions, and noise components. The green dashed lines indicate the input secular parallax amplitude of $78 \mu\text{as yr}^{-1}$. Top: the first point indicates a $\sim 10\sigma$ detection of the secular parallax amplitude. Note that only the first two distance cuts result in significant fits. Bottom: all fits are significant regardless of maximum distance cut. The uncertainties are similar to the first two points in the top plot (note that the axes scales are not the same).

nal to the expected secular parallax in all distance bins, and should therefore have nearly zero component in the fixed-direction fits. In Figure 9, we show the fixed-direction best-fit dipole amplitudes for D_{min} cuts be-

tween 1.5 and 35 Mpc, where we performed 50 trials per distance cut. Only $D_{min} < 5$ Mpc cuts result in significant detection of the secular parallax amplitude on average. The mean Z-scores of the fits for the two smallest D_{min} cuts are 9.5 and 8.0, respectively. For D_{min} cuts between 20 and 35 Mpc, typical Z-scores are 2. The prediction is therefore very sensitive to the inclusion of very nearby galaxies which have predicted parallaxes between 8 - 35 $\mu\text{as yr}^{-1}$. By comparison, D_{max} has little impact on the detection. Figure 9 also shows the best-fit dipole amplitudes for D_{max} cuts between 10 and 400 Mpc. We find that the best-fit dipole amplitude and Z-score are fairly constant for all D_{max} . The significance of the fits drops to $\sim 7\sigma$ for distance cuts < 20 Mpc, where the sample size is < 500 objects. Distant galaxies with large uncertainties compared to their expected parallax therefore have little impact on the detection as long as nearby objects with the most signal are included.

The G magnitude of each object impacts the simulated proper motions due to the dependence of the end-of-mission proper motion uncertainties on G . Magnitude vs. distance for each object are plotted in Figure 10, showing a tail of nearby, bright galaxies with $G < 15$. These objects will have the largest predicted proper motions and smallest uncertainties, provided that good astrometric solutions can be obtained for nearby, extended galaxies. The error-weighted fits are therefore highly sensitive to proper motions of these galaxies. We test this by varying the minimum G magnitude in the sample between 13 and 16 mag, and for each cut we perform 50 fits with resampled noise components. The best-fit dipole amplitudes are shown in Figure 10. We find that all fits including galaxies brighter than 15 mag are significant and consistent with secular parallax within 1σ . Relatively bright and nearby galaxies will most likely require closer individual inspection when real *Gaia* data is available in order to cull objects that may throw off the total fits due to spurious proper motions or larger than expected peculiar motions. The fact that some fits for G cuts < 15 are significant indicates that secular parallax may be detectable only if the majority of bright galaxies need not be culled. Nearby, diffuse galaxies will also require individual inspection, but they do not contribute to the measured signal as much as the brightest galaxies.

The mean noise-free proper motion is $\sim 1 \mu\text{as yr}^{-1}$ and the maximum is $65 \mu\text{as yr}^{-1}$, whereas the mean expected uncertainty is about $80 \mu\text{as yr}^{-1}$. The majority of simulated proper motions are then dominated by noise and vary greatly between trials. Controlling the maximum individual proper motion can therefore probe the dependence of the fits on noisy, insignificant

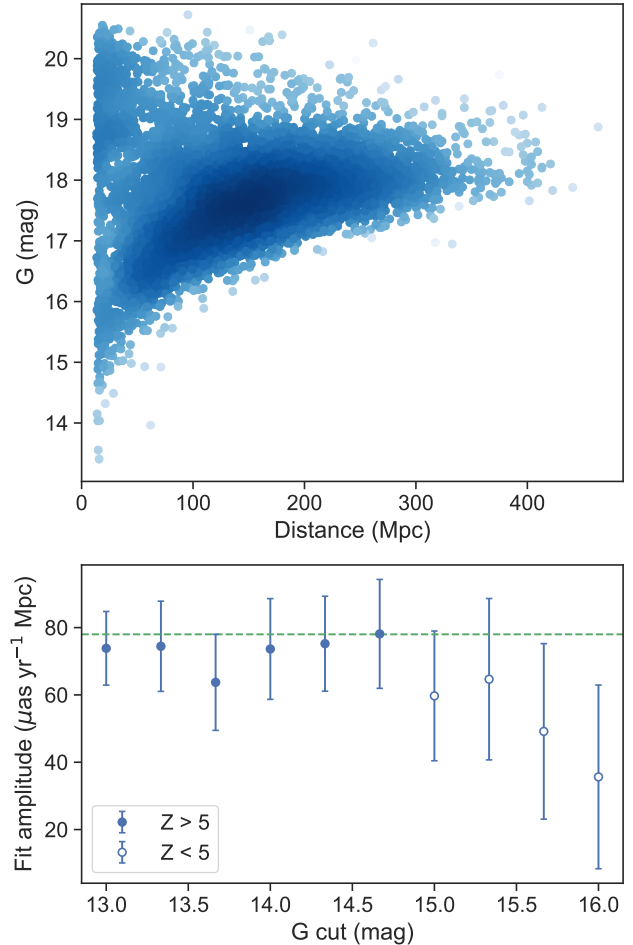


Figure 10. Top: G magnitudes vs. distance for *Gaia*-Cosmicflows galaxies. Predicted *Gaia* end-of-mission proper motion uncertainties scale with G . Bottom: simulated fixed-direction, distance-dependent dipole fits for minimum G magnitude cuts between 13 and 16 mag. The green dashed line indicates the input secular parallax amplitude of $78 \mu\text{as yr}^{-1}$. The first 6 cuts (minimum $G < 15$) result in significant average fits.

proper motions. In Figure 11, we plot the best-fit fixed-direction dipole amplitudes and Z-scores for maximum individual proper motion amplitude cuts up to $300 \mu\text{as yr}^{-1}$, where we have performed 50 trials per proper motion cut. New noise components are randomly generated for each trial, so the specific objects that are cut vary per trial. The best-fit dipole amplitude only depends on proper motion cut if the maximum proper motion is small enough so as to exclude nearby galaxies with the largest secular parallaxes. However, the significance of the fits is increased for cuts between 50 - $150 \mu\text{as yr}^{-1}$. Picking a proper motion cut in this range does not impact the previously established dependence on distance and magnitude cuts: the fits are still only significant if

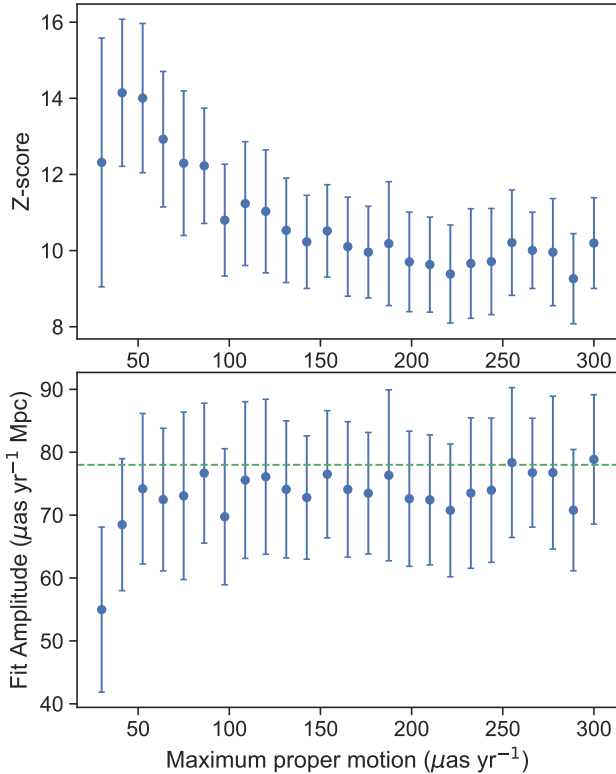


Figure 11. Z-scores (top) and best-fit amplitudes (bottom) of fixed-direction, distance-dependent dipole fits for maximum proper motion cuts up to $300 \mu\text{as yr}^{-1}$. The green dashed line indicates the input secular parallax amplitude of $78 \mu\text{as yr}^{-1}$.

relatively bright galaxies within 5 Mpc are included, but are insensitive to D_{max} .

5. LOW MULTIPOLE ANALYSIS OF PECULIAR PROPER MOTIONS

In this section, we study the predicted peculiar proper motions of Cosmicflows galaxies and compare to LSS theory. We also assess the impact that peculiar proper motions may have on quadrupole ($\ell = 2$) proper motion measurements, including gravitational waves and anisotropic expansion. In the following subsections, we utilize the simulated catalog described in Section 4.1 including only the peculiar velocity component of each galaxy’s proper motion.

5.1. Comparison to LSS Theory

Peculiar velocities arise from gravitational interactions with large-scale matter density fluctuations, causing transverse velocities, and therefore proper motions, of galaxies to deviate from a perfectly isotropic Hubble flow. Previous works (e.g. Darling & Truebenbach 2018 and Hall 2019) have demonstrated that extragalactic

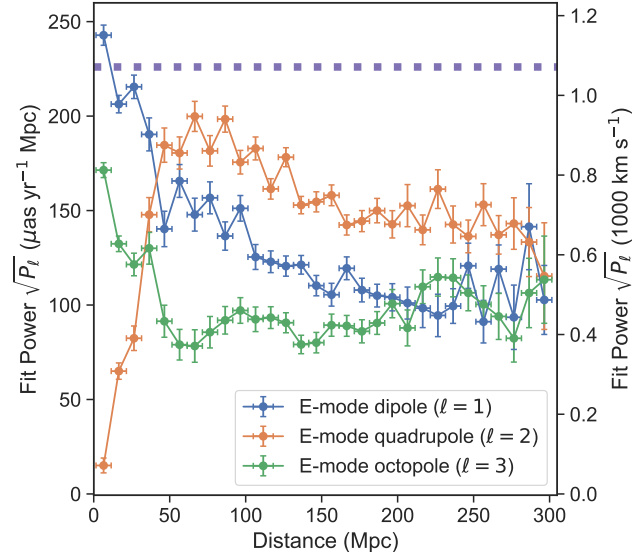


Figure 12. E-mode distance-dependent dipoles (blue), quadrupoles (orange), and octopoles (green) fit to the peculiar proper motions for objects in 10 Mpc distance bins up to 300 Mpc. The secular parallax power is indicated by the purple dashed line. The right vertical axis shows the same powers converted to distance independent velocities. Error bars represent the width of distance bins (horizontal) and the uncertainties of the fits (vertical), The fits were performed for noise-free modeled proper motions, so the fits and uncertainties are not indicative of expected *Gaia* end-of-mission results.

proper motions may probe these peculiar transverse velocities and therefore the matter power spectrum. Hall (2019) derive the peculiar velocity power spectrum for low redshift based on the matter power spectrum computed with the CAMB cosmology code. The peculiar velocity field is expected to be nearly curl-free and corresponds to an E-mode transverse velocity power spectrum where the dominant mode is distance dependent. Dipole correlations dominate for small distances, and the power transfers to higher ℓ (smaller angular scales) with increasing distance.

For comparison, in Figure 12 we show the E-mode dipole, quadrupole, and octopole square root powers ($\sqrt{P_\ell}$) fit to the noise-free model-predicted peculiar proper motions for 10 Mpc distance bins up to 300 Mpc, which gives an estimate of the power as a function of distance. The proper motion powers are normalized to 1 Mpc and can therefore be related to a transverse peculiar velocity, where a $1 \mu\text{as yr}^{-1}$ proper motion at 1 Mpc is equivalent to a $1 \text{ AU yr}^{-1} \approx 4.74 \text{ km s}^{-1}$ velocity. This method is equivalent to fitting distance-independent vector fields to the transverse velocities. The total velocity power in $\ell = 1, 2,$ and 3 is on the order of 1000 km s^{-1} at all distances. Square root pow-

ers should not be interpreted as representative proper motions or velocities. The amplitudes of the fits, however, represent the maximum magnitude of the vector field. For a dipole, the amplitude is simply proportional to the power, as given by Equation 4, but the amplitude for higher ℓ is not. We find the amplitude of each $\ell = 2, 3$ fit by solving numerically for the maximum of the best fit vector field magnitudes. The amplitudes of the highest power bins are 84, 88, and 80 $\mu\text{as yr}^{-1}$ Mpc, corresponding to velocities of 398, 417, and 380 km s^{-1} for $\ell = 1, 2$, and 3, respectively, roughly as expected for peculiar velocities induced by LSS.

As expected, the dipole power decreases with distance as the power shifts to the quadrupole, which peaks between 50-100 Mpc. The octopole power, however, does not match the theory predictions, since we see more power in the octopole than the quadrupole at small distances. This discrepancy may be due to uneven sky coverage of the galaxy sample. Alternatively, the octopole power may reflect real deviations of local matter density fluctuations, and therefore the peculiar velocity field, from universe-averaged models. We note, however, that the distance dependence of the peculiar proper motion power spectrum will not be detected using the *Gaia*-Cosmicflows sample. When *Gaia*-like noise is added to the proper motions, the power per distance bin is not significantly detected.

The secular parallax dipole power is $\sqrt{P_{E1}} = 226 \mu\text{as yr}^{-1}$ Mpc. While secular parallax decreases as $1/D$, the normalized power (which is a proxy for the solar system's linear velocity) is not a function of distance. Secular parallax is therefore dominant for distances $\gtrsim 40$ Mpc compared to the peculiar dipole. However, *Gaia* will not be sensitive enough to significantly detect secular parallax at that distance.

5.2. Impact on Distance-Independent Measurements

Cosmological effects such as the isotropy of the Hubble expansion and primordial gravitational waves induce distance-independent proper motion signals at low ℓ . Here we assess the impact that peculiar velocities will have on distance-independent proper motion quadrupole measurements. In comparison to the sample of local galaxies selected for this work, distance independent measures may be made for quasars at generally higher redshift. It is thus most relevant to compare the quadrupole powers recovered for large distance cuts, where we expect the LSS power spectrum to be dominated by higher ℓ . Figure 13 shows the results of simultaneously fitting an E-mode dipole and both E and B-mode quadrupoles to the noise-free peculiar proper motions for varying D_{min} . Note that these are distance-

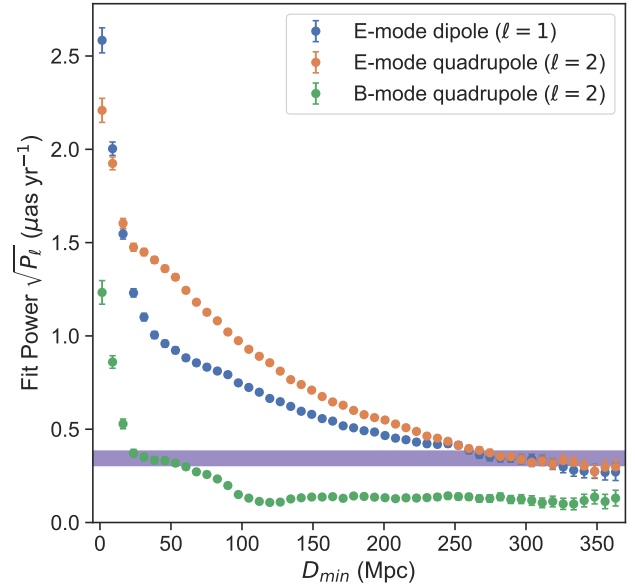


Figure 13. Distance-independent E-mode dipole (blue) and quadrupole (orange), and B-mode quadrupole (green) fits to the peculiar proper motions for varying minimum distances. The purple bar at $0.34 \mu\text{as yr}^{-1}$ represents the approximate total $\sqrt{P_2}$ (E2+B2) for $D_{min} > 300$ Mpc cuts.

independent fits, so the square root powers are 1-2 orders of magnitude lower than those in Figure 12 and cannot be simply scaled to a relative velocity. The powers in each mode approach minimum values $\sqrt{P_\ell} < 0.4 \mu\text{as yr}^{-1}$ for large distance cuts. Below, we describe the implications of these fit powers for measurements of the isotropy of the Hubble expansion and gravitational waves.

5.2.1. Anisotropic Expansion

Triaxial anisotropic expansion would be observable as an E-mode proper motion quadrupole, where galaxies appear to stream towards the directions of faster expansion (Darling 2014). The anisotropy is characterized by the fractional departure from the Hubble expansion in a given direction:

$$\Sigma_i = \frac{H_{i,0}}{H_0} - 1,$$

where i denotes the triaxial expansion axes x , y , and z . From Equations A1 and A2 of Darling (2014), we derive an expression to relate the total anisotropy to a proper motion quadrupole power by

$$\sqrt{P_{E_2}} = H_0 \sqrt{\frac{4\pi}{5} (\Sigma_x^2 + \Sigma_y^2 + \Sigma_z^2)}, \quad (7)$$

where H_0 is the Hubble constant expressed in units of proper motion, which we assume to be $H_0 \approx 70 \text{ km s}^{-1} \text{ Mpc}^{-1} = 15 \mu\text{as yr}^{-1}$.

The mean peculiar E-mode $\ell = 2$ power for $D_{min} > 300$ Mpc is $\sqrt{P_{E2}} = 0.3 \mu\text{as yr}^{-1}$, or 0.014 in units of $H_0\sqrt{4\pi/5}$. For each fit, we also solve for Σ_i using the relations to the quadrupole coefficients derived in Darling (2014). The average maximum anisotropy inferred from the quadrupole fits for $D_{min} > 300$ is $\Sigma_{max} \approx 0.01$. Anisotropic expansion would therefore be indistinguishable from LSS proper motions for anisotropy $< 1\%$. The predicted end-of-mission anisotropy noise floor for *Gaia* quasars is about 2% (roughly $\sqrt{P_{E2}} = 1 \mu\text{as yr}^{-1}$; Paine et al. 2018), so the anticipated limit on anisotropy from *Gaia* is unaffected by LSS. However, improved astrometric precision from a next generation Very Large Array (ngVLA) or future space based astrometry mission may enable quadrupole measurements with quasars that will approach or be limited by the LSS power.

5.2.2. Gravitational Waves

The primordial gravitational wave background will cause angular deflection of light rays with equal power in the E and B-modes for $\ell \geq 2$ (Gwinn et al. 1997; Book & Flanagan 2011), which may be observable as extragalactic proper motions. The power in $\ell = 2$ contributes 5/6 of the total gravitational wave signal, so the gravitational wave energy density may be estimated by

$$\Omega_{GW} = \frac{6}{5} \frac{1}{4\pi} \frac{P_2}{H_0^2}, \quad (8)$$

where P_2 is the total quadrupole power (E and B-modes). Darling et al. (2018) found astrometric limits on the gravitational wave energy density of $\Omega_{GW} < 0.0064$ for proper motions of 711 radio sources and $\Omega_{GW} < 0.011$ for proper motions of 508 radio sources combined with one epoch of *Gaia* data from the first data release. Additionally, they predicted a $\Omega_{GW} = 4 \times 10^{-4}$ noise floor for *Gaia* end-of-mission AGN proper motions.

For $D_{min} > 300$ the total quadrupole square root power approaches $\sqrt{P_2} = 0.34 \mu\text{as yr}^{-1}$, which corresponds to $\Omega_{GW} = 5 \times 10^{-4}$, similar to the predicted *Gaia* noise floor. However, the power in B2 is significantly lower than that in E2 for the peculiar proper motions, whereas gravitational waves produce equal power in E and B-modes. With improved astrometric precision, one may differentiate between the LSS quadrupole and gravitational waves by comparing the powers detected in the E and B-modes.

6. DISCUSSION AND CONCLUSIONS

The systematic errors of *Gaia* DR2 proper motions impose a noise floor that limits the amplitude of proper motion signals that may be studied with vector spheri-

cal harmonic decomposition. The large-scale systematics have been studied in detail by Lindegren et al. (2018) and *Gaia* Collaboration et al. (2018b), and correspond to $\sim 40 \mu\text{as yr}^{-1}$ for large angular scales. We find that the addition of distance data utilized in the secular parallax measurement, which one would not expect to be spatially correlated, does not allow us to probe signals below the systematic noise floor. We therefore find a $3500 \mu\text{as yr}^{-1}$ Mpc upper limit on the extragalactic secular parallax amplitude. Increased sample size would improve the sensitivity of the measurement since uncertainties scale as $N^{-1/2}$. However, achieving the statistical uncertainty to detect the $80 \mu\text{as yr}^{-1}$ Mpc signal of secular parallax using *Gaia* DR2 would require a sample size of $\sim 10^6$, which is more than the number of galaxies in the local volume.

Using the expected improvements to the sample size and proper motion uncertainties of *Gaia*-Cosmicflows galaxies in future data releases, we predict a significant (5-10 σ) detection of the secular parallax amplitude. This prediction is dependent on the assumption that the systematic errors in *Gaia* DR2 will be resolved. The detection is also highly sensitive to sample selection: relatively bright, local galaxies must be included to significantly detect secular parallax. We find that the secular parallax is only detected for simulations with D_{min} cuts < 5 Mpc and G magnitude cuts < 15 . The significance of the detection may also be improved by employing a proper motion amplitude cut $< 150 \mu\text{as yr}^{-1}$, which limits the portion of the sample with highly noise-dominated proper motions. Very distant galaxies with expected secular parallaxes well below *Gaia*'s expected proper motion precision may be included in the sample, but have little to no effect on the detected dipole as long as the signal is detected for local galaxies. *Gaia* data release 3 is expected to include results for extended objects and quasars, which may have implications for the secular parallax measurement.

The ultimate goal of a secular parallax measurement would be extragalactic distance estimates. However, the secular parallax may only be measured if a prior is assumed for the peculiar motion and distance, such as those provided by Cosmicflows-3, and therefore an independent distance estimate from secular parallax is most likely not possible for individual galaxies. Regardless, a statistical measurement of the secular parallax amplitude would lead to a constraint on the Hubble constant. If redshift is used as proxy for distance in Equation 1, then the amplitude of the fit is a product of the secular parallax proper motion amplitude and the local value of the Hubble parameter, H_0 . One therefore needs to either constrain the secular parallax amplitude or assume

the value from the CMB to infer the Hubble parameter. Our prediction does not directly translate to a redshift based fit because the galaxies closer than 5 Mpc that dominate the simulated fits most likely have large peculiar velocities relative to the recessional velocities predicted by the Hubble flow. However, the fit for nearby galaxies will be useful to assess the mixing of the secular parallax and peculiar dipole signals. From the results in Figure 9, we predict $\sim 2\sigma$ amplitude fits for D_{min} cuts > 20 Mpc, and thus a $\sim 2\sigma$ upper limit on H_0 if the secular parallax amplitude is assumed from the CMB dipole.

The primary limitation of the predicted detection and any resulting constraint on the Hubble constant is the dependence on very nearby galaxy proper motions, and thus the mixing of the secular parallax signal with the peculiar dipole. A potential method to improve the signal to noise at larger distances is to search for galaxy cluster members detected by *Gaia*. Individual proper motions could be averaged to determine the bulk motion of the cluster. Though cluster peculiar velocities are $\sim 500 \text{ km s}^{-1}$ (Planck Collaboration et al. 2018), the peculiar dipole would be lower in amplitude than the secular parallax for clusters at distances $\gtrsim 40$. After *Gaia*, astrometry from ngVLA or a future space based mission with lower per object uncertainties would improve the signal measured from more distant galaxies. Though an ngVLA quasar survey would miss many local galaxies observed by *Gaia*, the diminished peculiar dipole signal at the distances of relatively low redshift quasars may result in an improved constraint on the direction and amplitude of the secular parallax dipole.

Previous works have also made predictions of the secular parallax measurement with *Gaia*, namely, Ding & Croft (2009) and Hall (2019). Contrary to our results, neither work predicts a significant detection of the secular parallax. The discrepancy with our results are most likely due to differences in the samples used for predictions. Both Ding & Croft (2009) and Hall (2019) assume larger samples of more distant objects, whereas we find that significant secular parallax detection with *Gaia* is contingent on galaxies closer than ~ 5 Mpc. Our simulations excluding galaxies closer than at least 20 Mpc are consistent with previous works.

Our analysis of the Cosmicflows peculiar velocities are largely consistent with the LSS predictions of Hall (2019) though our methods of simulating the peculiar velocities are independent. The noise-free, Cosmicflows-based peculiar proper motions show a dominant dipole for low distances bins and power generally shifting to higher ℓ modes with increasing distance. We find that the peculiar proper motion dipole may be significantly detected with *Gaia* if one first detects or assumes the secular parallax dipole from the CMB. However, the distance dependence of the peculiar proper motion power spectrum will not be detectable with *Gaia*.

We demonstrated that the peculiar velocities also produce low multipole correlated proper motions that are distance independent, and therefore may impact other cosmological proper motion measurements made with quasars for signals of $\sim 0.3 \mu\text{as yr}^{-1}$. This would be indistinguishable from $\sim 1\%$ anisotropic expansion and would dominate the E-mode fields caused by a gravitational wave background. However, the gravitational wave energy density could still be constrained by studying the corresponding B-modes.

ACKNOWLEDGMENTS

We thank the anonymous referee for very helpful comments and corrections. The authors acknowledge support from the NSF Graduate Research Fellowship Program under grant DGE-1650115, the NSF grant AST-1411605, and the NASA grant 14-ATP14-0086. RG acknowledges support from the European Research Council (ERC) under the European Unions Horizon 2020 research and innovation programme (grant agreement no759194 - USNAC). This work has made use of data from the European Space Agency (ESA) mission *Gaia* (<https://www.cosmos.esa.int/gaia>), processed by the *Gaia* Data Processing and Analysis Consortium (DPAC, <https://www.cosmos.esa.int/web/gaia/dpac/consortium>). Funding for the DPAC has been provided by national institutions, in particular the institutions participating in the *Gaia* Multilateral Agreement.

Software: astropy (Astropy Collaboration et al. 2013), pyGaia, TOPCAT (Taylor 2005)

REFERENCES

- Astropy Collaboration, Robitaille, T. P., Tollerud, E. J., et al. 2013, A&A, 558, A33, doi: 10.1051/0004-6361/201322068
- Bachchan, R. K., Hobbs, D., & Lindegren, L. 2016, A&A, 589, A71, doi: 10.1051/0004-6361/201527935
- Book, L. G., & Flanagan, É. É. 2011, PhRvD, 83, 024024, doi: 10.1103/PhysRevD.83.024024

- Darling, J. 2014, MNRAS, 442, L66,
doi: [10.1093/mnras/slu057](https://doi.org/10.1093/mnras/slu057)
- Darling, J., & Truebenbach, A. E. 2018, ApJ, 864, 37,
doi: [10.3847/1538-4357/aad3d0](https://doi.org/10.3847/1538-4357/aad3d0)
- Darling, J., Truebenbach, A. E., & Paine, J. 2018, ApJ, 861, 113, doi: [10.3847/1538-4357/aac772](https://doi.org/10.3847/1538-4357/aac772)
- Ding, F., & Croft, R. A. C. 2009, MNRAS, 397, 1739,
doi: [10.1111/j.1365-2966.2009.15111.x](https://doi.org/10.1111/j.1365-2966.2009.15111.x)
- Djorgovski, S., & Davis, M. 1987, ApJ, 313, 59,
doi: [10.1086/164948](https://doi.org/10.1086/164948)
- Dressler, A., Lynden-Bell, D., Burstein, D., et al. 1987,
ApJ, 313, 42, doi: [10.1086/164947](https://doi.org/10.1086/164947)
- Gaia Collaboration, Prusti, T., de Bruijne, J. H. J., et al. 2016, A&A, 595, A1, doi: [10.1051/0004-6361/201629272](https://doi.org/10.1051/0004-6361/201629272)
- Gaia Collaboration, Brown, A. G. A., Vallenari, A., et al. 2018a, A&A, 616, A1, doi: [10.1051/0004-6361/201833051](https://doi.org/10.1051/0004-6361/201833051)
- Gaia Collaboration, Mignard, F., Klioner, S. A., et al. 2018b, A&A, 616, A14,
doi: [10.1051/0004-6361/201832916](https://doi.org/10.1051/0004-6361/201832916)
- Graziani, R., Courtois, H. M., Lavaux, G., et al. 2019,
MNRAS, 488, 5438, doi: [10.1093/mnras/stz078](https://doi.org/10.1093/mnras/stz078)
- Gwinn, C. R., Eubanks, T. M., Pyne, T., Birkinshaw, M., & Matsakis, D. N. 1997, ApJ, 485, 87, doi: [10.1086/304424](https://doi.org/10.1086/304424)
- Hall, A. 2019, MNRAS, 486, 145,
doi: [10.1093/mnras/stz648](https://doi.org/10.1093/mnras/stz648)
- Hinshaw, G., Weiland, J. L., Hill, R. S., et al. 2009, ApJS, 180, 225, doi: [10.1088/0067-0049/180/2/225](https://doi.org/10.1088/0067-0049/180/2/225)
- Hogg, D. W. 1999, arXiv e-prints, astro.
<https://arxiv.org/abs/astro-ph/9905116>
- Kardashev, N. S. 1986, AZh, 63, 845
- Lindgren, L., Hernández, J., Bombrun, A., et al. 2018,
A&A, 616, A2, doi: [10.1051/0004-6361/201832727](https://doi.org/10.1051/0004-6361/201832727)
- Mignard, F., & Klioner, S. 2012, A&A, 547, A59,
doi: [10.1051/0004-6361/201219927](https://doi.org/10.1051/0004-6361/201219927)
- Paine, J., Darling, J., & Truebenbach, A. 2018, ApJS, 236, 37, doi: [10.3847/1538-4365/aabe2d](https://doi.org/10.3847/1538-4365/aabe2d)
- Planck Collaboration, Aghanim, N., Akrami, Y., et al. 2018, A&A, 617, A48, doi: [10.1051/0004-6361/201731489](https://doi.org/10.1051/0004-6361/201731489)
- Taylor, M. B. 2005, Astronomical Society of the Pacific Conference Series, Vol. 347, TOPCAT & STIL: Starlink Table/VOTable Processing Software, ed. P. Shopbell, M. Britton, & R. Ebert, 29
- Titov, O., & Lambert, S. 2013, A&A, 559, A95,
doi: [10.1051/0004-6361/201321806](https://doi.org/10.1051/0004-6361/201321806)
- Truebenbach, A. E., & Darling, J. 2017, ApJS, 233, 3,
doi: [10.3847/1538-4365/aa9026](https://doi.org/10.3847/1538-4365/aa9026)
- Tully, R. B., Courtois, H. M., & Sorce, J. G. 2016, AJ, 152, 50, doi: [10.3847/0004-6256/152/2/50](https://doi.org/10.3847/0004-6256/152/2/50)
- Tully, R. B., & Fisher, J. R. 1977, A&A, 500, 105

APPENDIX

1. GALAXIES

Galaxies in the *Gaia*-Cosmicflows crossmatch were each visually inspected for features that would indicate a poor *Gaia* fit, as discussed in Section 3.1.1. Figures 14-21 show images of the 232 galaxies used for the parallax limit in Section 3.2. SDSS *g*-band images are shown where available, otherwise the images are DSS2 red-band. Several galaxies are located near the edge of the SDSS plate, in which case we reviewed additional images in the literature, but we display the truncated SDSS images in Figures 14-21.

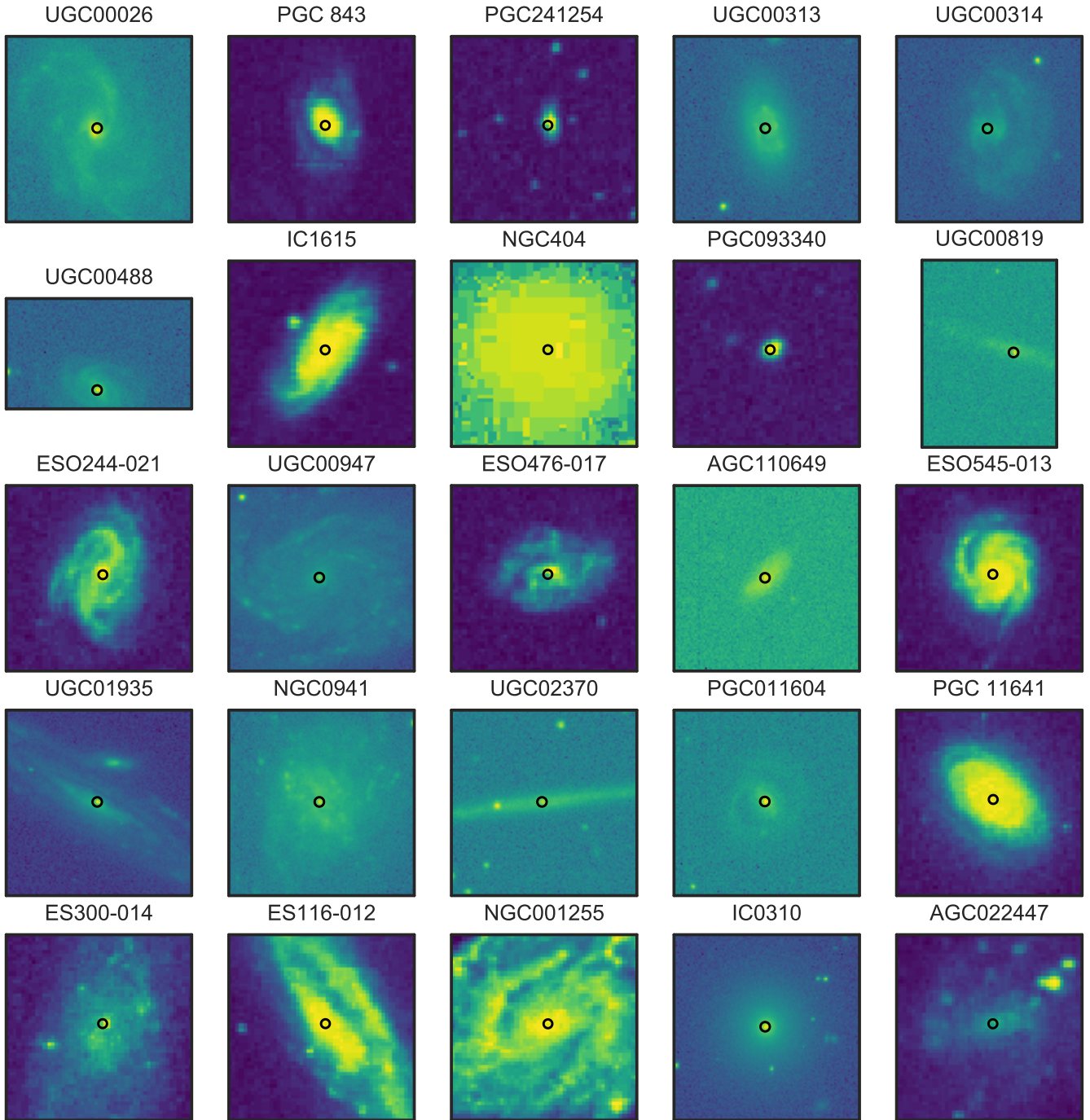


Figure 14. SDSS g-band or DSS2 red-band imaging for galaxies selected to attempt detection of the secular parallax dipole.

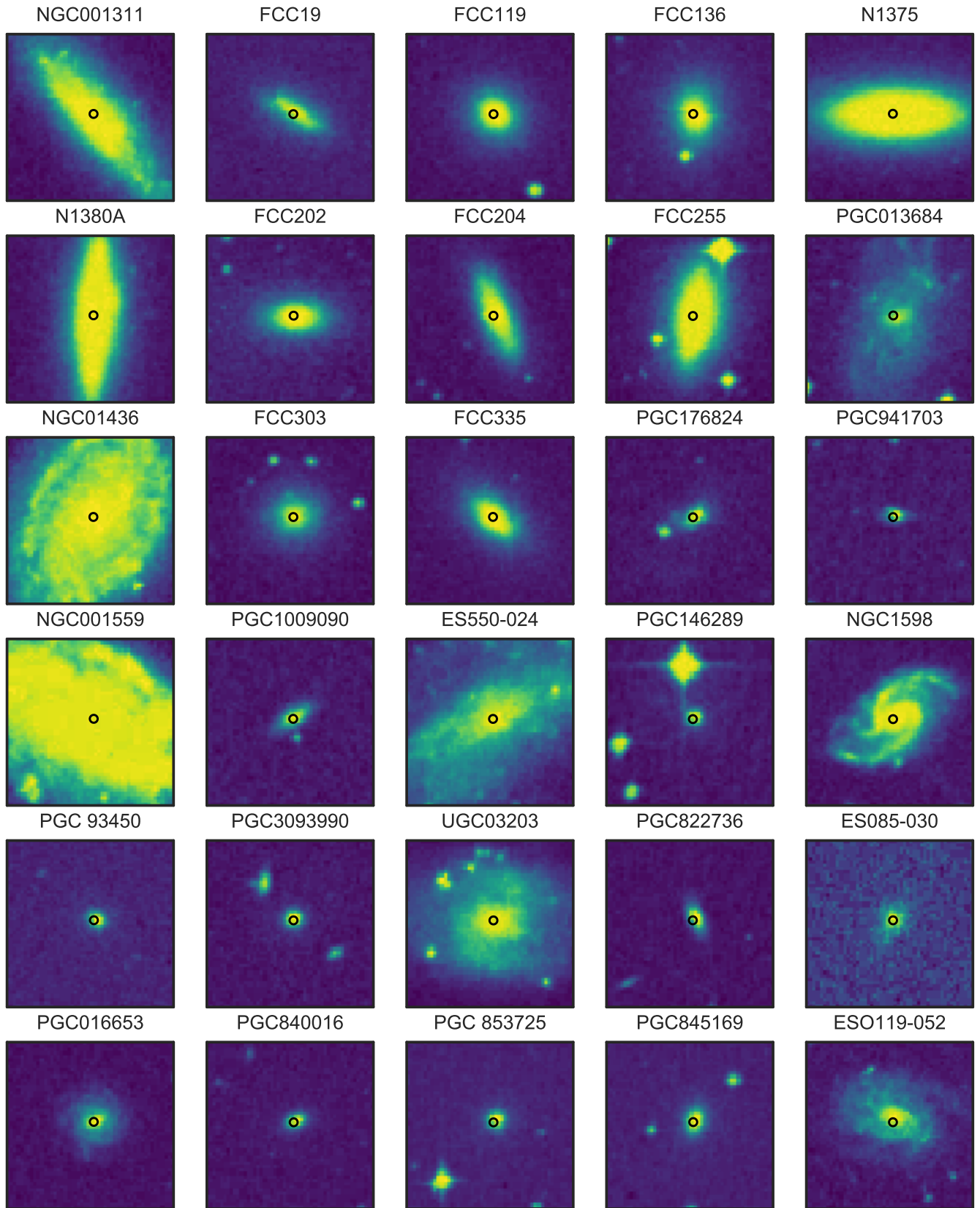


Figure 15. Continued from Figure 14.

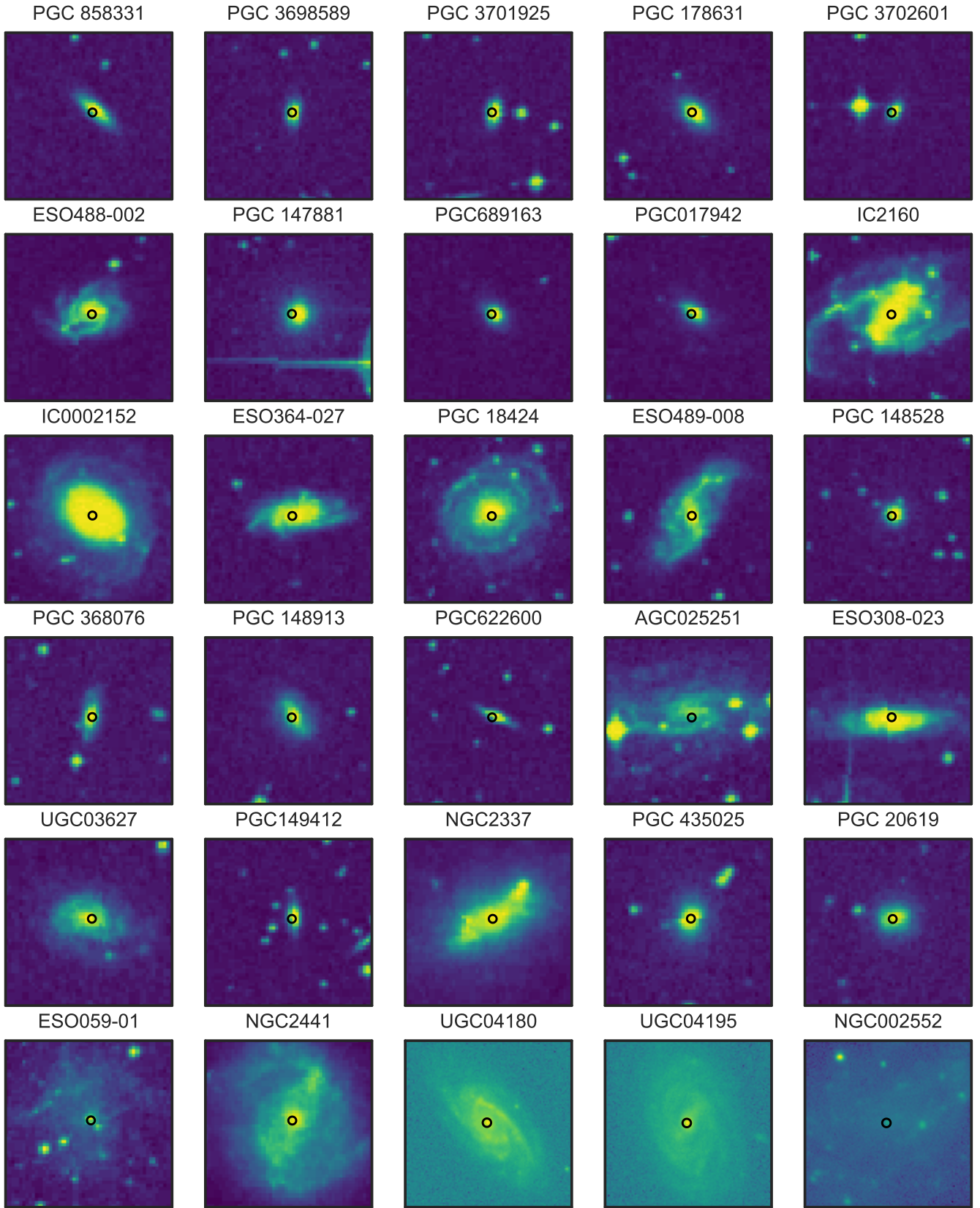


Figure 16. Continued from Figure 15.

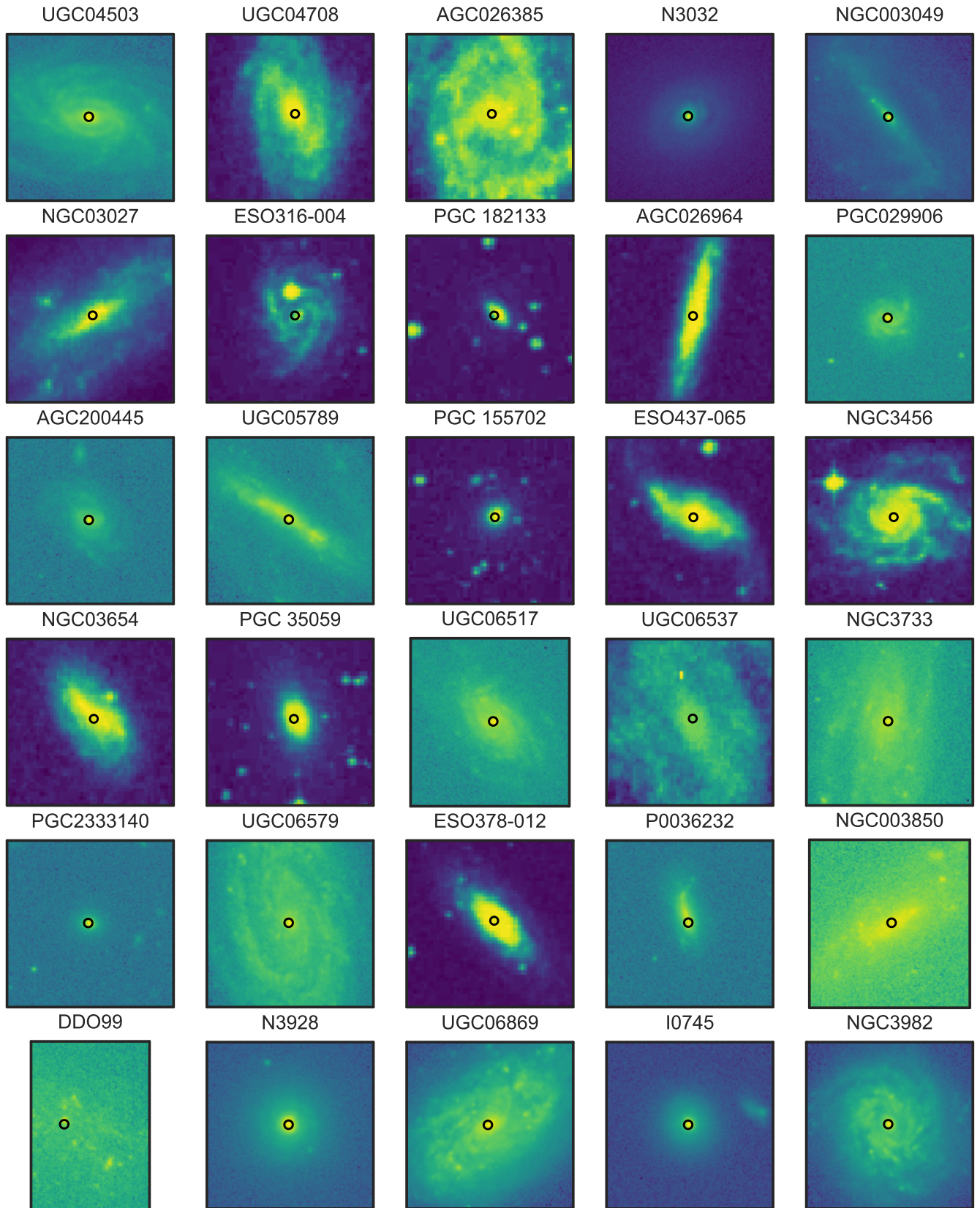


Figure 17. Continued from Figure 16.

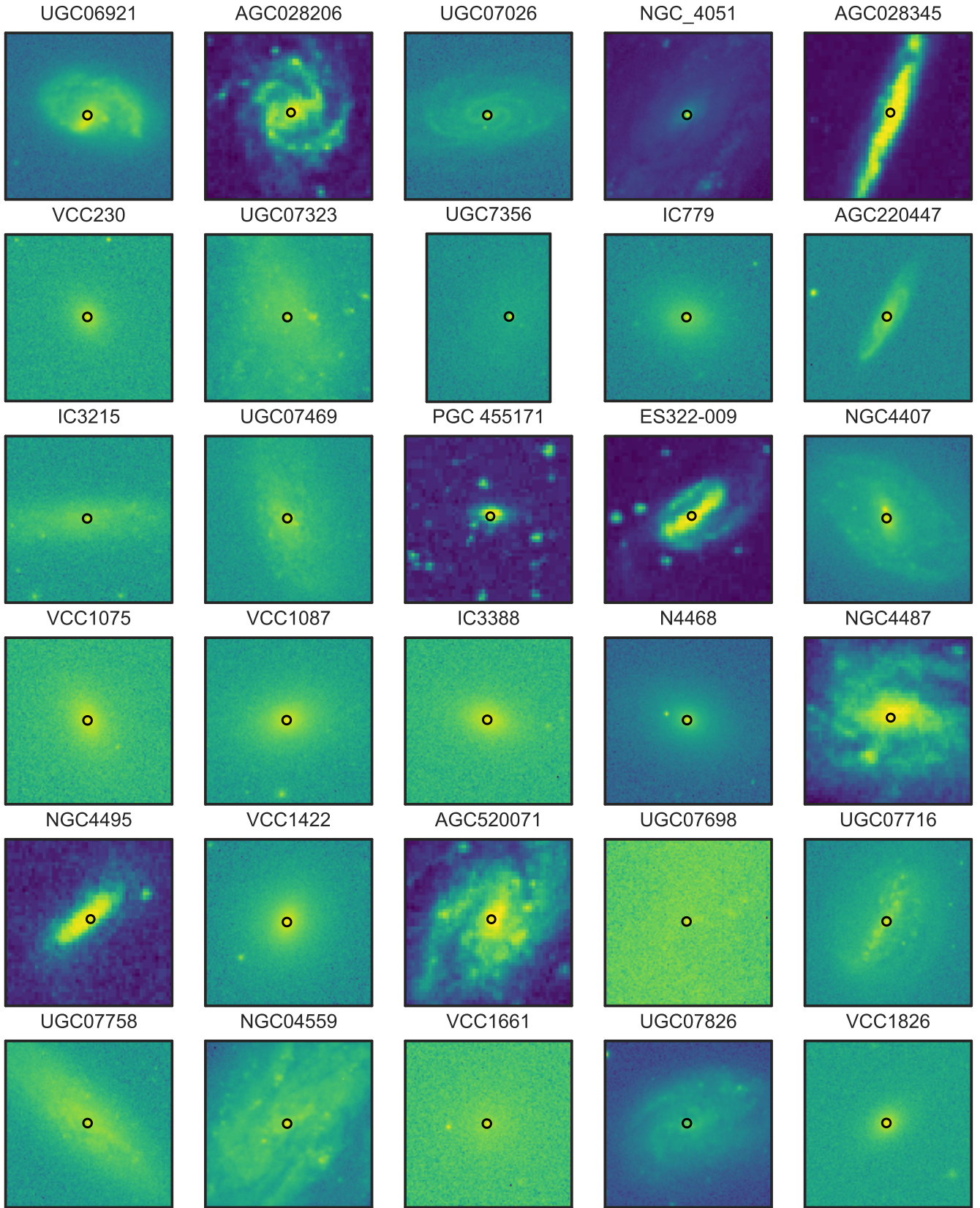


Figure 18. Continued from Figure 17.

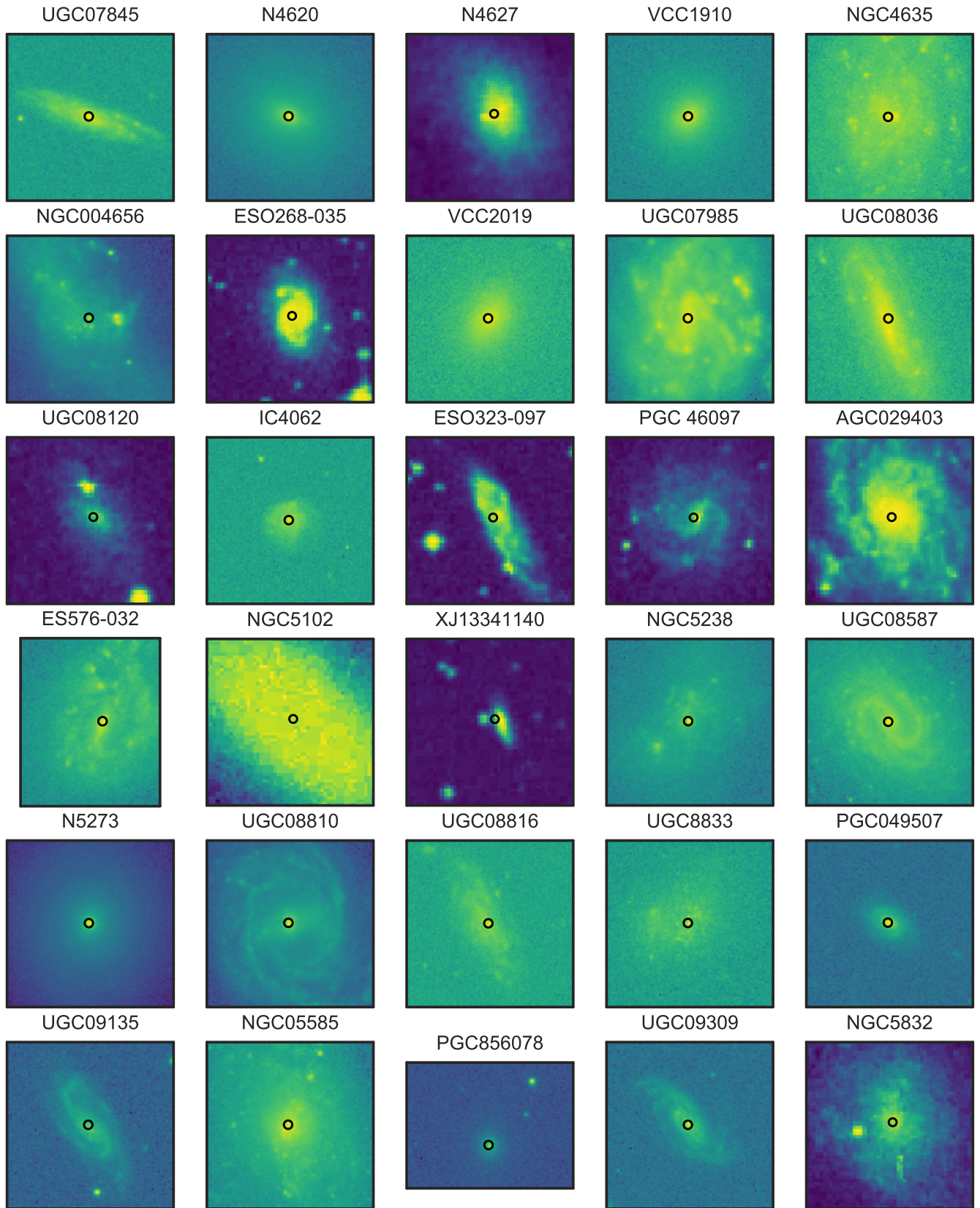


Figure 19. Continued from Figure 18.

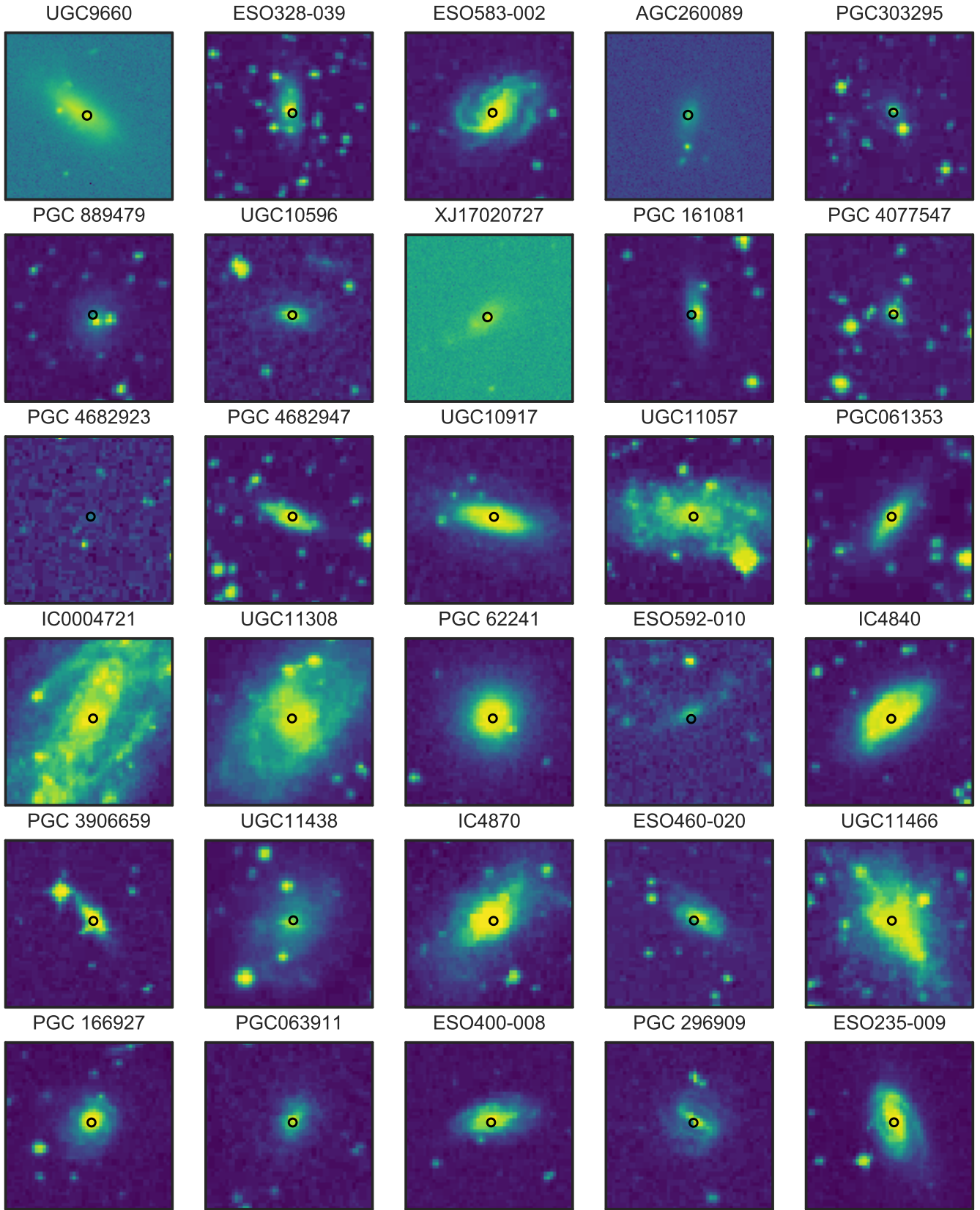


Figure 20. Continued from Figure 19.

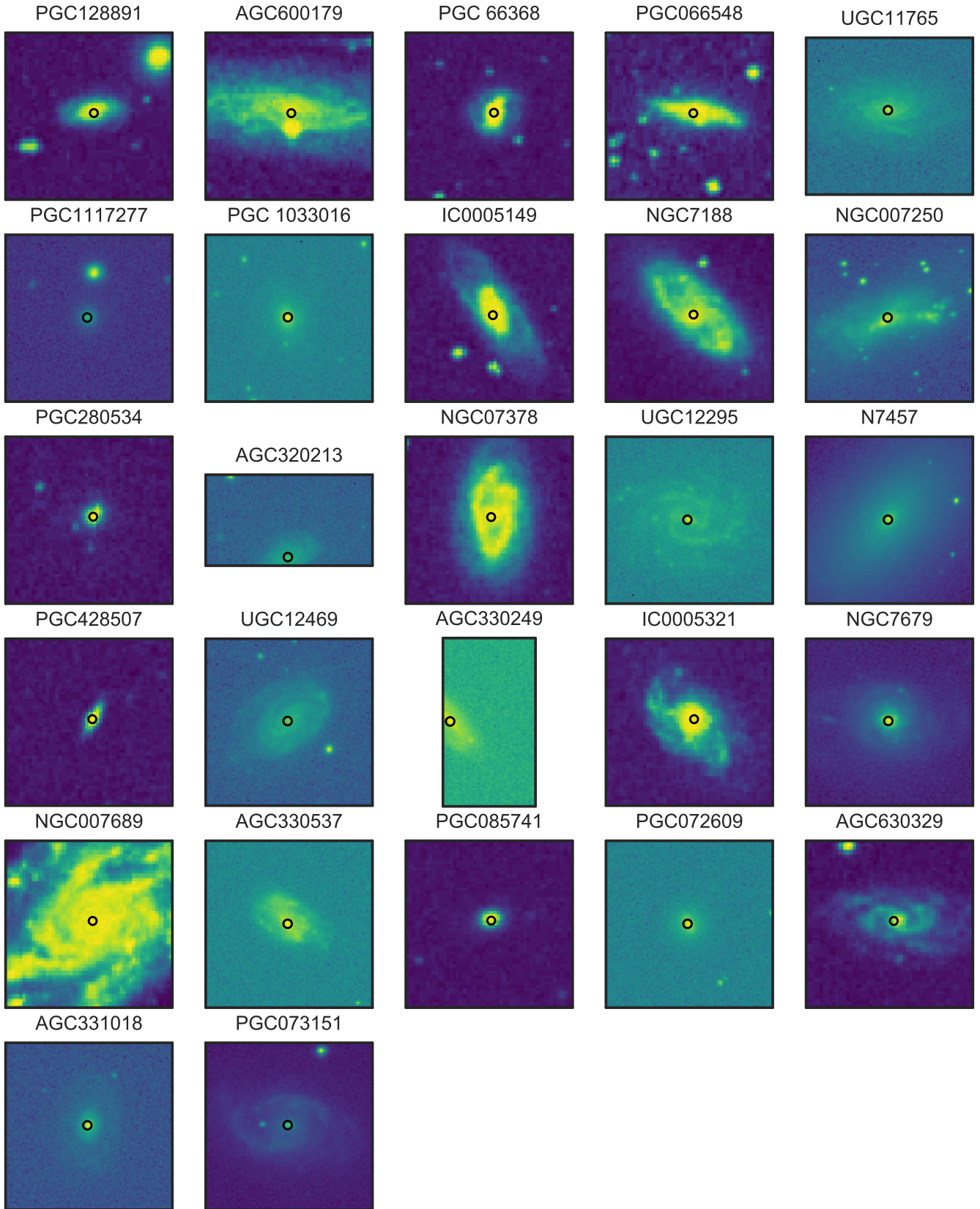


Figure 21. Continued from Figure 20.